

PROBING QUARK-GLUON PLASMA BY MEASUREMENT OF STRANGE
CHARM MESONS PRODUCTION IN pp AND $PbPb$ COLLISIONS WITH CMS
DETECTOR

A Dissertation

Submitted to the Faculty

of

Purdue University

by

Cheng-Chieh Peng

In Partial Fulfillment of the
Requirements for the Degree

of

Doctor of Philosophy

May 2020

Purdue University

West Lafayette, Indiana

THE PURDUE UNIVERSITY GRADUATE SCHOOL
STATEMENT OF DISSERTATION APPROVAL

Dr. Wei Xie, Chair

Department of Physics and Astronomy

Dr. Fuqiang Wang

Department of Physics and Astronomy

Dr. Denes Molnar

Department of Physics and Astronomy

Dr. Luis Martin Kruczynski

Department of Physics and Astronomy

Approved by:

Dr. John P. Finley

Head of the Department of Physics and Astronomy

TABLE OF CONTENTS

	Page
LIST OF TABLES	v
LIST OF FIGURES	vi
ABSTRACT	x
1 INTRODUCTION	1
1.1 Quantum Chromodynamics	1
1.1.1 QCD Phase Diagram	2
1.2 Heavy Flavor Quarks in QGP	3
1.3 Strangeness Production in QGP	4
2 LHC COLLIDER AND CMS DETECTOR and CMS Detector	6
2.1 The Large Hadron Collider (LHC)	6
2.2 The Compact Muon Solenoid Detector (CMS)	7
2.2.1 Tracking System	8
3 DATASETS AND EVENT SELECTIONS	12
3.1 Datasets	12
3.2 Trigger and Event Selection	13
3.3 Signal Monte Carlo	14
3.3.1 Weight for MC Sample	14
3.3.2 MC D_s^+ Decay Length Tuning	18
4 D_S^\pm RECONSTRUCTION AND SIGNAL EXTRACTION	20
4.1 D_S^\pm Reconstruction	20
4.2 Selection Cut Optimization	22
4.3 Signal Extraction	26
4.4 $D_S^\pm \rightarrow \phi\pi^\pm$ Channel Ratio Extraction	32
4.5 Acceptance and Efficiency Correction	34
4.6 Nonprompt D_S^\pm Estimation	36
5 SYSTEMATIC UNCERTAINTIES	40
5.1 Summary of Systematic Uncertainties on the Proton-Proton Cross Section	40
5.2 Summary of Systematic Uncertainties on the PbPb dN/dp_T	42
5.3 Summary of Systematic Uncertainties on the Nuclear Modification Factor	44
5.4 Summary of Systematic Uncertainties on the Ratio of D_s^+ over D^0	46

	Page
5.5 Systematics Associated with Selection Efficiency	49
5.6 Systematics Associated with Signal Extraction	58
5.7 Systematic Associated with MC D_s^+ p_T Shape	65
5.8 Systematic Associated with Non-prompt Ds	65
6 RESULTS AND SUMMARY	67
6.1 Results	67
6.2 Summary	70
REFERENCES	72

LIST OF TABLES

Table	Page
3.1 Summary of HLT paths used in the pp and PbPb analysis.	13
3.2 D_s^+ p_T and \hat{p}_T threshold and number of events for MC samples	15
4.1 Track selection criteria for pp and PbPb events.	21
4.2 Summary table of the selection criteria in different p_T intervals.	23
4.3 Branching ratio of B mesons to D mesons.	37
5.1 Summary of relative systematics (%) for 5.02 TeV pp collisions.	41
5.2 Summary of relative systematics (%) for 5.02 TeV PbPb collisions.	42
5.3 Summary of relative systematics (%) for the nuclear modification factor in pp and PbPb collisions at $\sqrt{s_{\text{NN}}} = 5$ TeV	44
5.4 Summary of relative systematics (%) for D_s^+ over D^0 ratio in pp collisions at $\sqrt{s} = 5.02$ TeV.	46
5.5 Summary of relative systematics (%) for D_s^+ over D^0 ratio in PbPb collisions at $\sqrt{s_{\text{NN}}} = 5.02$ TeV	47
5.6 Summary of relative systematics (%) for selection efficiency in pp collisions.	50
5.7 Summary of relative systematics (%) for selection efficiency in PbPb collisions.	50
5.8 Relative systematics (%) for non-prompt D_s^+ in pp collisions.	66
5.9 Relative systematics (%) for non-prompt D_s^+ in PbPb collisions.	66

LIST OF FIGURES

Figure	Page
1.1 A schematic view of QCD phase diagram (7).	3
1.2 Nuclear modification factor measurements of light (17), charm (12) and beauty (18; 19) hadrons with CMS detector in PbPb collisions at $\sqrt{s_{NN}} = 5.02$ TeV.	4
1.3 B_s^0/B^+ R_{AA} ratio measurement with CMS detector (27) in PbPb collisions at $\sqrt{s_{NN}} = 5.02$ TeV.	5
2.1 Schematic view of the LHC injector chain (29).	7
2.2 Cartoon of the CMS detector (31)	8
2.3 Particle flow at CMS detector (31)	9
2.4 Schematic view of CMS tracker system.	10
2.5 Resolution in longitudinal coordinate of hits in the barrel of the pixel detector. The incident angle is the angle of the track relative to the normal to the plane of the sensor.	11
2.6 p_T resolution of tracks as a function of pseudorapidity (left) and as function of p_T (right).	11
3.1 MC sample enhancement weight v.s. D_s^+ p_T	16
3.2 Weighted MC D_s^+ p_T distributions	17
3.3 Weighted PbPb MC D_s^+ p_T distributions v.s hiBin.	17
3.4 Comparison of D_s^+ decay length error distribution of Data and MC. The left pannel is with no MC scale. The right pannel is with the best MC scale.	19
3.5 The best MC decay length error scale in pp (left) and PbPb (right), the error is estimated by taking the scale with $\chi^2 = \chi_{Best}^2 + 1$	19
4.1 Statistical significance $S/\sqrt{S+B}$ versus signal efficiency for pp collision events. Vertical lines indicate the optimized cut.	24
4.2 Statistical significance $S/\sqrt{S+B}$ versus signal efficiency for PbPb collision events. Vertical lines indicate the optimized cut.	25

Figure	Page
4.3 The mass distribution of D_s^+ to : $\phi(\rightarrow K^+K^-)\pi^+$, $f_0(\rightarrow K^+K^-\pi^+)$, $\bar{K}^*(\rightarrow K^-\pi^+)K^+$ with generated-matched signal and the D_s^+ signal with correct track collection but wrong mass assignment. <i>Left</i> : Invariant mass of K^+K^- pair. <i>Right</i> : Invariant mass of $K^+K^-\pi^+$, with the ϕ mass window selection applied.	26
4.4 Double Gaussian fit for pp (top) and PbPb (bottom) signal MC in $p_T = 6 - 8$ (left) and $20 - 40$ GeV (right).	28
4.5 Invariant mass distribution of D_s^+ candidates with p_T from 2 to 6 GeV/ c in pp collisions at $\sqrt{s}=5.02$ TeV with signal extraction fitting curve. The blue dashed line represents the background fit, while the red solid line represents the signal plus the background fit.	29
4.6 Invariant mass distribution of D_s^+ candidates with p_T from 6 to 8 GeV/ c in pp collisions at $\sqrt{s}=5.02$ TeV with signal extraction fitting curve. The blue dashed line represents the background fit, while the red solid line represents the signal plus the background fit.	30
4.7 Invariant mass distribution of D_s^+ candidates with p_T from 6 to 8 GeV/ c in PbPb collisions at $\sqrt{s_{NN}}=5.02$ TeV with signal extraction fitting curve. The blue dashed line represents the background fit, while the red solid line represents the signal plus the background fit.	31
4.8 Fitting plot of invariant mass of K^+K^- in pp. <i>Left</i> : MC. <i>Right</i> : data.	32
4.9 Fitting plot of invariant mass of K^+K^- in PbPb. <i>Left</i> : MC. <i>Right</i> : Data.	33
4.10 Prompt D_s^+ (red) and nonprompt D_s^+ (blue) to $\phi\pi^\pm$ acceptance (left), and acceptance times total efficiency (right) for pp collision at $\sqrt{s}=5.02$ TeV.	34
4.11 Prompt D_s^+ (red) and nonprompt D_s^+ (blue) to $\phi\pi^\pm$ acceptance (left), and acceptance times total efficiency (right) for PbPb collision at $\sqrt{s_{NN}}=5.02$ TeV.	35
4.12 B mesons fraction v.s rapidity at different collision energy by PYTHIA simulation.	38
4.13 <i>Left</i> : normalized p_T distribution of nonprompt D_s^+ and D^0 from PYTHIA 8 MC. <i>Right</i> : the ratio of nonprompt D_s^+ over nonprompt D^0 in the analysis p_T bins.	38
4.14 Estimated p_T differential cross section of nonprompt D_s^+ in pp collision (left), and dN/dp_T of nonprompt D_s^+ in PbPb collision (right).	39
4.15 Fraction of prompt D_s^+ differential cross sections to all D_s^+	39

Figure	Page
5.1 Summary of relative systematics (%) for 5.02 TeV pp collisions.	41
5.2 Summary of relative systematics (%) for 5.02 TeV PbPb collisions.	43
5.3 Summary of relative systematics (%) for nuclear modification collisions.	45
5.4 Summary of relative systematics (%) for D_s^+ over D^0 ratio in pp and PbPb collisions.	48
5.5 Vertex probability scan for D_s^+ with p_T range from 2 to 6 GeV/ c in pp collisions, where the y-axis is the cross section ratio of varied cut to default cut. The blue dashed line indicate the default cut used in the analysis. The red dashed line is the linear fit of the data.	51
5.6 Vertex probability scan for D_s^+ with p_T range from 6 to 40 GeV/ c in pp collisions, where the y-axis is the cross section ratio of varied cut to default cut. The blue dashed line indicate the default cut used in the analysis. The red dashed line is the linear fit of the data.	52
5.7 Vertex probability scan for D_s^+ with p_T range from 6 to 40 GeV/ c in PbPb collisions, where the y-axis is the cross section ratio of varied cut to default cut. The blue dashed line indicate the default cut used in the analysis. The red dashed line is the linear fit of the data.	53
5.8 D_s^+ pointing angle distribution in data and MC (pp). Bottom panels: the ratio of data to MC.	54
5.9 D_s^+ pointing angle distribution in data and MC (PbPb). Bottom panels: the ratio of data to MC.	55
5.10 D_s^+ decay length significance in data and MC (pp). Bottom panels: the ratio of data to MC.	56
5.11 D_s^+ decay length significance in data and MC (PbPb). Bottom panels: the ratio of data to MC.	57
5.12 Signal extraction fit in pp collisions for D_s^+ p_T 2 to 6 GeV/ c with second-order Chebyshev polynomial for background.	59
5.13 Signal extraction fit in pp collisions for D_s^+ p_T 6 to 40 GeV/ c with second-order Chebyshev polynomial for background.	60
5.14 Signal extraction fit in PbPb collisions for D_s^+ p_T 6 to 40 GeV/ c . Third-order Chebyshev polynomial for background in p_T : 6-8 and 8-10 GeV/ c bins, and Second-order for background in p_T : 10-20 and 20-40 GeV/ c bins	61
5.15 Signal extraction fit in pp collisions for D_s^+ p_T 2 to 6 GeV/ c with single-Gaussian fit for Signal.	62

Figure	Page
5.16 Signal extraction fit in pp collisions for D_s^+ p_T 6 to 40 GeV/ c with single-Gaussian fit for Signal.	63
5.17 Signal extraction fit in PbPb collisions for D_s^+ p_T 6 to 40 GeV/ c with single-Gaussian fit for Signal.	64
5.18 Ratio of efficiency for alternative weight to default weight for prompt D_s^+ (Red), non-prompt D_s^+ (blue) in pp(left) and PbPb(right) collisions.	65
6.1 $\frac{d\sigma}{dp_T}$ in pp and $\frac{1}{T_{AA}} \frac{dN}{dp_T}$ in PbPb at $\sqrt{s_{NN}} = 5.02$ TeV. The colored boxes represent the systematic uncertainty.	68
6.2 Nuclear modification factor (R_{AA}) of D_s^+ mesons in PbPb collisions at $\sqrt{s_{NN}} = 5.02$ TeV. The Magenta line represents the PHSD(43), the parton-hadron-string dynamics transport model including a contribution of hadronisation via quark recombination, prediction.	69
6.3 D_s^+/D^0 Ratio in pp and PbPb at $\sqrt{s_{NN}} = 5.02$ TeV. The lower panel shows the double ratio of D_s^+/D^0 in PbPb over in pp. The green line represents the TAMU(58), while the violet (magenta) line represnet the PHSD pp (PbPb) prediction.	70

ABSTRACT

Peng, Cheng-Chieh Ph.D., Purdue University, May 2020. Probing Quark-Gluon Plasma By Measurement of Strange Charm Mesons Production in pp and PbPb Collisions with CMS Detector. Major Professor: Wei Xie.

This thesis presents the first measurement of prompt D_s^+ mesons in heavy ion collisions with the CMS experiment. The transverse momentum (p_T) spectra of prompt D_s^+ mesons and charge conjugates are measured in pp and PbPb collisions at a center-of-mass energy of 5.02 TeV per nucleon pair using the CMS detector at the LHC. The measurement is performed through the $D_s^+ \rightarrow \phi\pi^+ \rightarrow K^+K^-\pi^+$ decay channel with the D_s^+ rapidity range $|y| < 1.0$. The D_s^+ production in the p_T range from 2 (6) GeV/c to 40 GeV/c in pp (PbPb) collisions is measured. Suppression of the D_s^+ nuclear modification factor (R_{AA}) in PbPb collisions suggests a significant interaction between charm quarks and the quark-gluon plasma. The double ratio of prompt D_s^+ to prompt D^0 production in pp and PbPb is measured. The ratio is consistent with a PHSD model calculation and consistent with unity, which indicates that strange charm meson enhancement in PbPb collisions is not found in the measured p_T interval.

1. INTRODUCTION

The universe is widely believed to have begun with the Big Bang. For a few millionths of a second after this singularity, the universe was like a soup filled with extremely hot and dense matter. Based on the asymptotic freedom property (1; 2) of quantum chromodynamics (QCD), quarks and gluons are liberated to move freely on their own under the conditions. This phenomenon, which is very different from the world we are familiar with today, where all color objects are confined and cannot be directly observed, is called "Quark Gluon Plasma" (QGP).

The study of QGP is one of the fundamental pieces in understanding the universe. To create such extreme conditions for QGP to exist, physicists have proposed accelerating heavy ions to relativistically high energy and make them collide head-on. Where a significant amount of energy is deposited in a minuscule "fireball" with extremely high temperature, such the condition for creating QGP. Currently, there are two major colliders performing such kind of experiments: the Relativistic Heavy Ion Collider (RHIC) at Brookhaven National Laboratory (BNL) and the Large Hadron Collider (LHC) at the European Organization for Nuclear Research (CERN). RHIC uses deuterium, gold and copper ion beams to collide around $\sqrt{s_{NN}} = 200$ GeV, while LHC can achieve ten times or more energy per nucleon with proton or lead collisions. Evidences for the existence of QGP has been found by RHIC experiments (3; 4) and later has also been observed at LHC (5; 6).

1.1 Quantum Chromodynamics

According to the Standard Model of particle physics, our world consists of three generations of quarks, lepton and the recent founded Higgs boson with four kinds of fundamental interaction mediated by different gauge bosons. The strong interaction

is one of these interactions, which is the strongest at short-range and holds quarks together to form hadrons. The relativistic quantum field theory to describe the strong interaction is called Quantum Chromodynamics (QCD).

Like in Quantum Electrodynamics, in QCD there is also a "charge" called "*color*". There are three basic color states for quarks, which are usually labeled with red, green and blue. These three color states form a basis in a 3-dimensional complex vector space on which gauge transformations can act according to the SU(3) group.

Based on the symmetry of SU(3) group, there should be 9 kinds of gluons, the mediator of the strong interaction, including eight color octet states, and one state is color singlet. However, the color singlet could be exchanged between two color singlets which could happen as a long-range force. Since we do not observe this long-range gluon interaction, it indicates only color octet gluons exist.

One of the remarkable features of QCD is asymptotic freedom: the strong interaction coupling constant α_s gets weaker at shorter range, or with larger momentum transfer. From the one-loop renormalization group equation, the α_s is given as:

$$\alpha_s = \frac{12\pi}{(33 - 2N_f)\ln(Q^2/\Lambda_{QCD}^2)} \quad (1.1)$$

where N_f is the number of effectively massless quark flavors, Q^2 is the square of four-momentum transfer and Λ_{QCD} is the QCD scale constant whose value has to be determined by experiment. From the equation, α_s is not a constant but instead varies with Q^2 . In the case of $Q^2 \rightarrow \infty$, α_s is approaching to zero.

1.1.1 QCD Phase Diagram

A schematic view of QCD phase diagram is shown in Fig.1.1. Heavy-ion collisions make collision happen at low baryon density and high energy to reach the QGP regime. On the phase diagram, another interesting phase is the "*Color Superconductor*", which occurs at low temperature and very large baryon density. In this phase, quarks form "*Cooper pair*" analogize to the superconductivity in condensed matter physics. Based on Lattice QCD calculations (8), the phase transition at low baryon

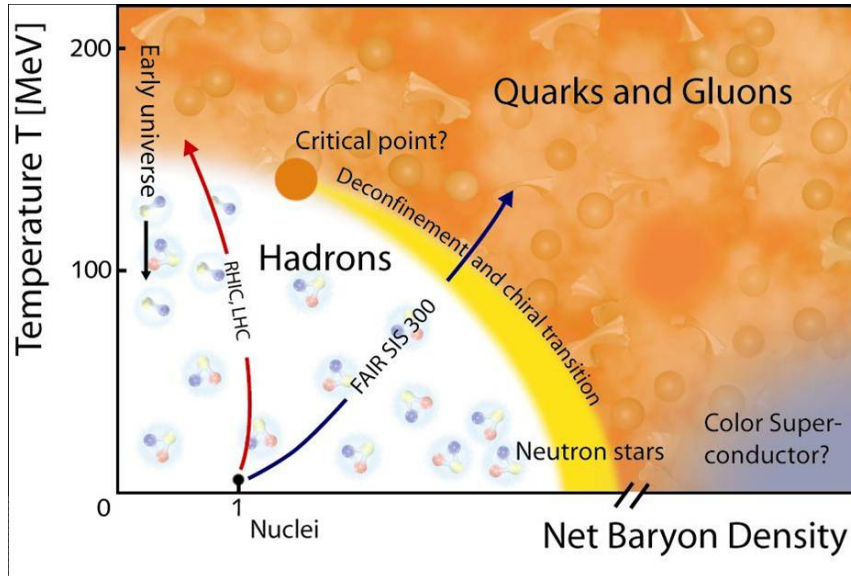


Figure 1.1. A schematic view of QCD phase diagram (7).

density with temperature going up is a cross-over, without any discontinuity. This also indicates the existence of a critical point where the first-order phase transition happens (shows in Fig 1.1).

1.2 Heavy Flavor Quarks in QGP

The study of heavy-quark production plays a crucial role in understanding the mechanisms of heavy-quark interaction with the medium created in heavy-ion collisions. Heavy quarks are primarily produced at early stages of heavy-ion collisions due to its large mass. Therefore they carry information about the pre-thermalization properties of the quark gluon plasma. Compared with light quarks and gluons, heavy quarks are expected to lose less energy due to smaller color charge and the dead cone effect (9). Detailed measurements of both production and collectivity for charm and bottom hadrons can supply information crucial to understanding the properties of the strongly interacting QCD matter.

Evidence of a strong charm meson suppression in heavy-ion collisions with respect to the corresponding pp references is observed by ALICE (10; 11), CMS (12) at LHC and STAR (13) at RHIC, while a hint of a smaller suppression of D^0 with respect to charged particles is observed at low p_T . The measurement of D^0 azimuthal anisotropy suggests a strong interaction between charm quarks and the medium (14; 15; 16).

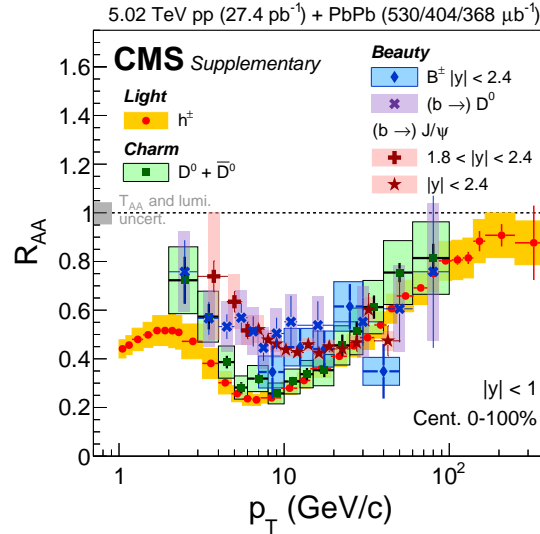


Figure 1.2. Nuclear modification factor measurements of light (17), charm (12) and beauty (18; 19) hadrons with CMS detector in PbPb collisions at $\sqrt{s_{NN}} = 5.02$ TeV.

1.3 Strangeness Production in QGP

With the predicted chiral symmetry restoration, strangeness production is expected to be enhanced (20). This phenomenon is studied using measurements of strange hadrons performed at STAR in CuCu, AuAu (21; ?) and at ALICE in PbPb (23) collisions. It was proposed that coalescence of quarks plays an important role in heavy quark hadronization at low momentum in heavy-ion collisions (?; ?). The production of D_s^+ mesons is expected to be enhanced in the strangeness-

rich QGP (?). The measurement of the production cross section in this thesis could provide essential information for the heavy quark hadronization mechanisms in QGP.

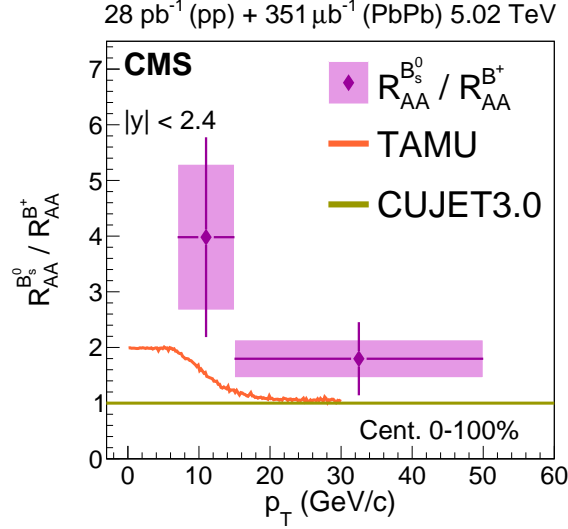


Figure 1.3. B_s^0/B^+ R_{AA} ratio measurement with CMS detector (27) in PbPb collisions at $\sqrt{s_{NN}} = 5.02$ TeV.

The measurements of B_s^0/B^+ (27) and Λ_c^+/D^0 (28) cross section ratio in pp and PbPb collisions reveal a hint of the strange heavy flavor meson enhancement and baryon enhancement with quark coalescence. In this thesis, the production of prompt D_s^+ and its charge conjugates D_s^- (This analysis does not distinguish between the charge conjugates) in pp and PbPb collisions in 2015 at 5.02 TeV with the CMS detector is presented with the transverse momentum range from 2 (pp) or 6 (PbPb) GeV/c to 40 GeV/c. The measurements of D_s^+ in pp collisions provide the baseline information for coalescence and fragmentation.

2. LHC COLLIDER AND CMS DETECTOR and CMS Detector

In this thesis, the measurement is performed on the data generated at the LHC and collected at the CMS detector. Basic information of these experiment apparatus is described in this chapter.

2.1 The Large Hadron Collider (LHC)

The Large Hadron Collider (LHC) (29) consist of a 27 kilometer two-ring superconducting hadron accelerator and collider at CERN. The project was approved by the CERN Council in December 1994 aimed for built with a \sqrt{s} (center of mass of energy) up to 14 TeV collision in pp collisions and $\sqrt{s_{NN}} \simeq$ (center of mass of energy per nucleon) 5.5 TeV for PbPb collisions.

The accelerator complex is shown in Fig.2.1. Lead ions start their path at ECR (electron cyclotron resonance), then pass through a series of accelerators and spectrometer to fed into the CERN Low Energy Ion Ring (LEIR). LEIR is used to transform a set of low-intensity ion pulses into shorter bunches with higher intensity. The bunches are then sent to CERN PS (Proton Synchrotron), accelerated to 5.9 GeV and stripped fully to Pb^{82+} . These ions are then sent to the SPS and injected into the LHC rings.

On the LHC rings, there are seven detectors constructed at intersection points include two general-purpose detectors: ATLAS (30) and CMS (31) and one detector specifically designed for studying QGP: ALICE (32). During the collision stage, opposite directions of beams are tuned to cross at small angle (120 to 150 microradians) at collision point.

The first heavy-ion run started in November 2010 with PbPb collisions at $\sqrt{s_{NN}} = 2.76$ TeV. Up to year of 2018, LHC has collected pPb, PbPb data at both $\sqrt{s_{NN}} = 2.76$ TeV and 5.02 TeV together with corresponding pp collision reference.

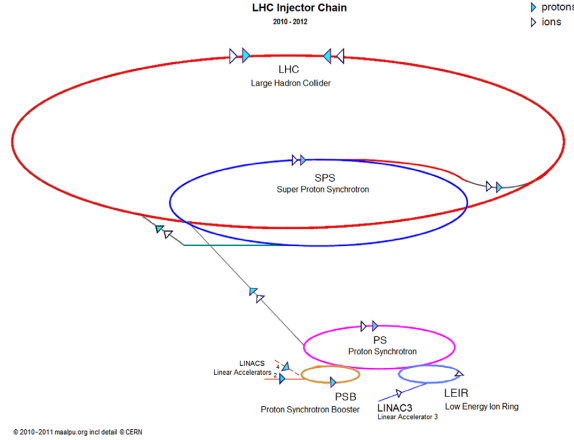


Figure 2.1. Schematic view of the LHC injector chain (29).

2.2 The Compact Muon Solenoid Detector (CMS)

The CMS detector is a general-purpose apparatus at interaction point 5 at LHC. It is composed of multi sub-detectors for detection of different type of objects. Figure 2.2 shows the layout of CMS detector, and Figure 2.3 demonstrate how different particle travel and interact with sub-detectors. From innermost to outermost is : the silicon tracking system which record hit from charged particle and can be used to reconstruct charged particle trajectory; the lead tungstate crystal in electromagnetic calorimeter (ECAL) scintillates when photon or electron pass through it, and photodetectors collect the emitted photon to measure the energy; Similar to ECAL, the brass and scintillator hadron calorimeter (HCAL) measured the energy of hadrons; the superconducting solenoid is designed to provide a uniform 4-T magnetic field inside and 2-T magnetic field in the muon chamber with 4 layers of return yoke.

A detailed description of the CMS experiment can be found in Ref. (31).

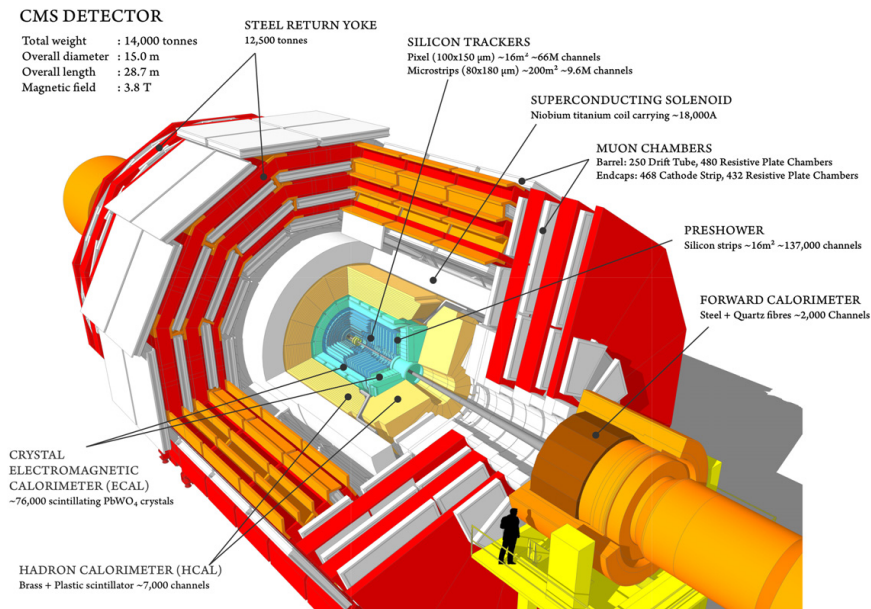


Figure 2.2. Cartoon of the CMS detector (31)

2.2.1 Tracking System

The tracker system is designed to measure charged particles within the pseudorapidity range $|\eta| < 2.5$. It has a cylindrical volume 5.8 m in length and 2.5 m in diameter. Figure 2.4 shows a schematic view of the CMS tracker. The tracker consisted of two part. The innermost part to the interaction point (IP) is 1440 modules of silicon pixel detector which has three layers at radii between 4.4 cm and 10.2 cm in the barrel region and two pairs of endcap disks at ± 34.5 cm and ± 46.5 cm. The position resolution is approximately $10 \mu\text{m}$ in the transverse and 20–40 in the longitudinal coordinate (see Figure 2.5). The outer part is 15 148 silicon modules of silicon strip detector. The strip tracker is composed of four subsystem based on its

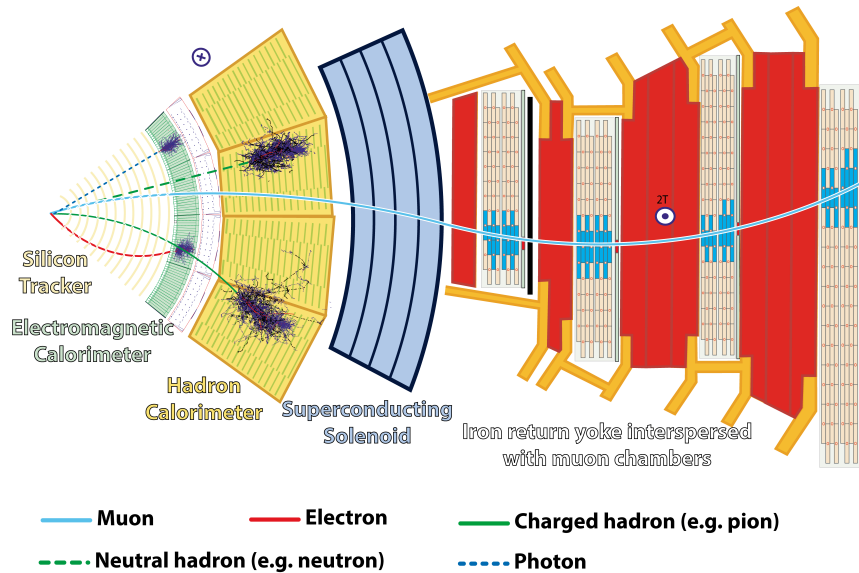


Figure 2.3. Particle flow at CMS detector (31)

relative position to IP, including the Tracker Inner Barrel (TIB) and Disks (TID), the Tracker Outer Barrel (TOB), and the Tracker EndCaps (TEC).

The track reconstruction is made by feeding the local hits reconstruction to Combinatorial Track Finder (CTF), which is an adaptation of the combinatorial Kalman filter(33) with extension to allow pattern recognition and track fitting. It runs through several iterations, starting with finding interaction point and then the displaced tracks and also recover tracks not found in the previous iterations. Each iteration proceeds in four steps :

- Seed generation provides initial track candidates found using only a few hits.
- Track finding based on a Kalman filter with seed for finding hits in extrapolated trajectories.
- The track-fitting is used to provide the best estimate of the parameters of each trajectory.
- Track selection set quality flag, and discards tracks that fail certain criteria. With current configuration of tracker systems layer and reconstruction algorithm, the track

resolution are typically typically 1.5% in p_T and 25–90 (45–150) μm in the transverse (longitudinal) impact parameter. The tracking resolution performances are shown in Figure 2.6. Further details for tracking system and its performance in Ref (34).

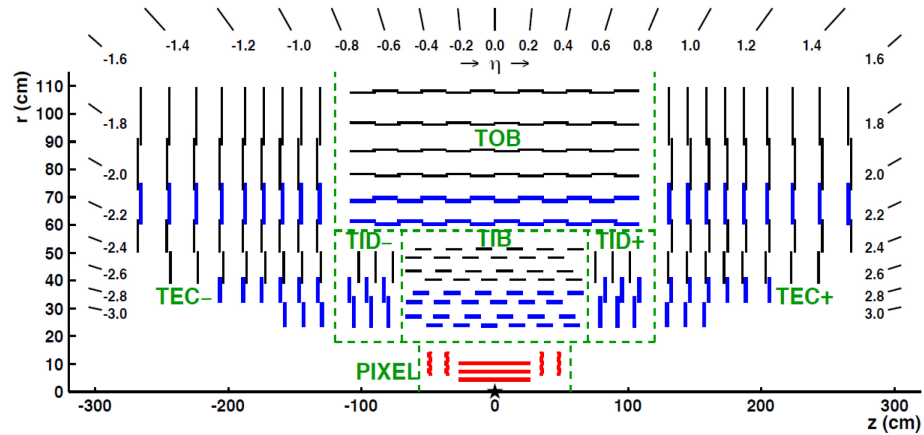


Figure 2.4. Schematic view of CMS tracker system.

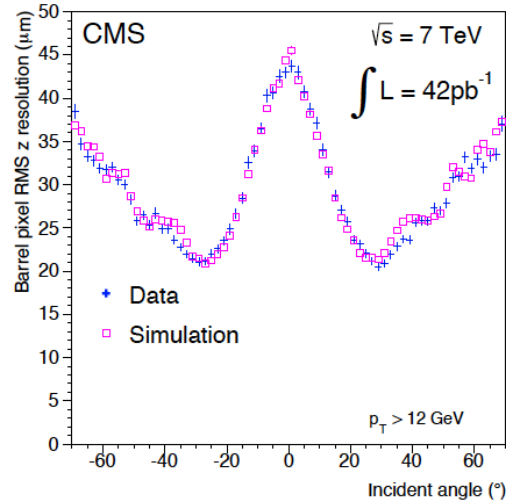


Figure 2.5. Resolution in longitudinal coordinate of hits in the barrel of the pixel detector. The incident angle is the angle of the track relative to the normal to the plane of the sensor.

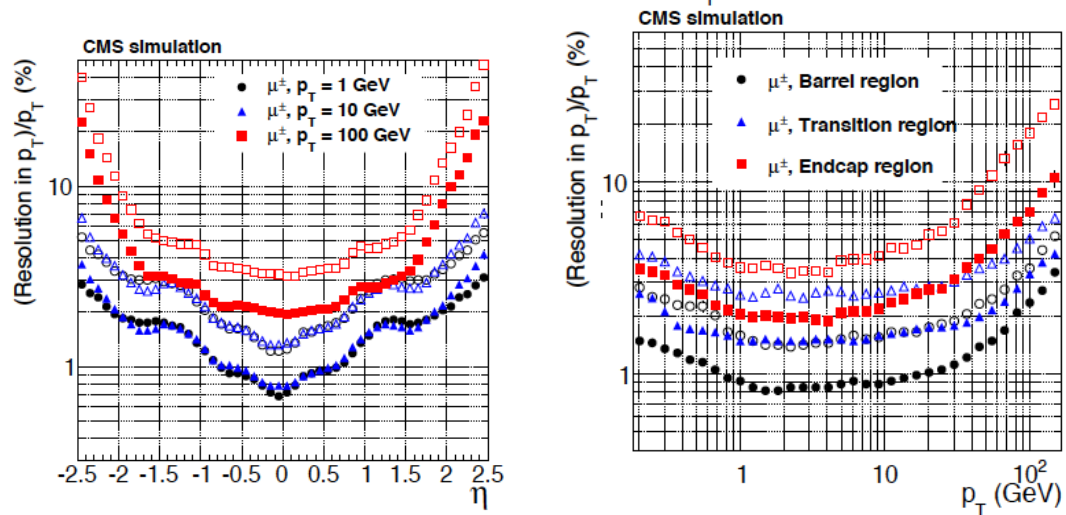


Figure 2.6. p_T resolution of tracks as a function of pseudorapidity (left) and as function of p_T (right).

3. DATASETS AND EVENT SELECTIONS

In this chapter, the dataset and MC used in this analysis is described.

3.1 Datasets

This analysis is performed using the 2015 pp and PbPb collision data at $\sqrt{s_{\text{NN}}} = 5.02$ TeV. The integrated luminosity for pp sample is 38.1 nb^{-1} (from golden JSON runs), while for PbPb sample is $43.9 \mu\text{b}^{-1}$ ($21.64 \mu\text{b}^{-1}$ from the golden JSON runs and $22.22 \mu\text{b}^{-1}$ from the TrackOnly JSON runs). Details of the dataset are summarized in Table 3.1.

Sample	Luminosity	DAS name
pp	38.1 nb^{-1}	/MinimumBias1-20/Run2015E-PromptReco-v1/AOD
PbPb	$43.9 \mu\text{b}^{-1}$	/HIMinimumBias1-11/HIRun2015-PromptReco-v1/AOD

During the LHC runs, experimentalists monitor the conditions of each sub detector both on-line and off-line to ensure the data is collected correctly. If all sub-detectors works normally, the runs will be certified as good and included into golden JSON. During 2015 PbPb run, there was a water leakage accident happened, affecting some of CMS sub-detectors for some runs. The TrackOnly JSON marks those data collected at that period of time, in which the tracker system was working normally. Since in this analysis the needed physics objects are solely reconstructed via tracker system, adding TrackOnly JSON runs could greatly enhance the total statistics. Good quality of the data is ensured by applying the JSON files for pp and PbPb respectively:

- *Cert_262081 – 262328_5TeV_PromptReco_Collisions15_25ns_JSON.txt*
- *Cert_262548 – 263757_PromptReco_HICollisions15_JSON_v2_PbPb.txt*

- *Cert_263685 – 263757_PromptReco_HICollisions15_TrackerOnly_JSON.txt*

Both pp and PbPb samples were reconstructed using the CMSSW (CMS Software framework) version CMSSW_7_5_8.

3.2 Trigger and Event Selection

Minimum-bias trigger is used for this analysis. The trigger path is listed in Table 3.1. Details of minimum-bias triggers are described in (35). The minimum-bias pp sample corresponds to about 2.67 billion events, while the PbPb minimum-bias sample to about 294 million events.

Table 3.1.
Summary of HLT paths used in the pp and PbPb analysis.

DataSet	HLT trigger
pp	HLTL1MinimumBiasHF1OR_part*_v1
PbPb	HLTL1MinimBiasHF2AND_part*_v1

In the offline analysis, additional event selections are applied to reduce background processes (beam-gas collisions) as described in Ref. (17). Both pp and PbPb events are required to have at least one reconstructed primary vertex within 15 cm from the center of nominal collision point along the beam axis and less than 0.15 cm in the transverse plane. For PbPb collisions, a coincidence of at least three towers in each HF calorimeter, with more than 3 GeV of total energy, from the HF detectors on both sides of the interaction point is required. Also, the shape of the cluster in the pixel detector in PbPb collision has to be compatible with the expectation Ref. (36).

3.3 Signal Monte Carlo

Prompt and non-prompt D_s^+ Monte Carlo samples were produced to estimate acceptance and selection efficiencies, and to evaluate the systematic uncertainties. The samples were generated by PYTHIA8 (37) Tune CUEP8M1 at 5.02 TeV. D_s^+ mesons are further forced to decay through these three channels : $\phi(\rightarrow K^+K^-)\pi^+$, $f_0(980)(\rightarrow K^+K^-)\pi^+$ and $\bar{K}^*(\rightarrow K^-\pi^+)K^+$, by the EVTGEN package (38), in which final state radiations are generated using PHOTOS (39). Only events with at least one D_s^+ with $|y| < 1.2$ and $|\eta| < 2.4$ were kept. MC events were generated with different D_s^+ p_T thresholds, and the \hat{p}_T thresholds were used to speed up the PYTHIA production while keeping the sample unbiased. Details of MC p_T and \hat{p}_T thresholds with sample size are listed in Table 3.2. For PbPb production, selected PYTHIA events were embedded into a simulated PbPb background generated by HYDJET (version 1.8 , tune "Cymbal5Ev8") (40).

3.3.1 Weight for MC Sample

The MC samples are first merged with a sample enhancement weight due to D_s^+ p_T thresholds to restore the default PYTHIA p_T distributions. The enhancement weights are shown in Fig. 3.1. To have a better match with real data, two kinds of p_T weights are further applied. A weight based on measured D^0 spectra (41) is firstly used , then the prompt D_s^+ are weighted based on the measured result, as default for this analysis. Another weight based on FONLL calculation (42) is used for systematical uncertainties.

The weight procedure is similar to that in nonprompt D^0 measurement (41). Both prompt and non-prompt D_s^+ MC samples are first weighted to FONLL p_T distribution then weighted to real data by the ratio between them. For prompt D_s^+ , since the FONLL only provides the D^0 distribution, the m_T -scaling method is applied ($m_{D_s^+}^2 + p_{T,D_s^+}^2 = m_{D^0}^2 + p_{T,D^0}^2$) to transform it to D_s^+ distribution. The obtained p_T distributions are compared to measured results then use the ratio as additional weight

Table 3.2.

 D_s^+ p_T and \hat{p}_T threshold and number of events for MC samples

	threshold (GeV)					
$D_s^+ p_T$	0	1.9	3.8	5.7	9.5	19
\hat{p}_T	0	0	0.3	2	3.5	9
Channel	number of MC events					
pp						
All Channel	500k	1M	300k	300k	100k	50k
PbPb						
Prompt $\phi \pi$	1M	2M	500k	500k	150k	80k
Prompt f0 π	500k	1M	300k	300k	100k	75k
Prompt $K^* K$	500k	1M	300k	300k	100k	75k
NonPrompt $\phi \pi$	1M	2M	400k	400k	150k	50k
NonPrompt f0 π	500k	1M	300k	300k	100k	50k
NonPrompt $K^* K$	500k	1M	300k	300k	100k	50k

to better match with Data. For non-prompt D_s^+ , the p_T weight is done on ancestor B p_T instead of the non-prompt D_s^+ , otherwise the p_T relation for $B \rightarrow D_s^+$ decay will be destroyed.

For PbPb MC, additional weight proportional to the number of binary collisions is applied to account the fact that the MC is produced by embedding one PYTHIA D_s^+ events into HYDJET background, while in data the probability to produce a D_s^+ meson is enhanced with the number of binary collisions. For the FONLL based weight, to consider the nuclear modification factor effect on particle productions, theoretical predictions from PHSD (43) and TAMU (44; 45) are applied to prompt and nonprompt D_s^+ respectively.

The weighted MC $D_s^+ p_T$ distributions are shown in Fig. 3.2, Fig. 3.3.

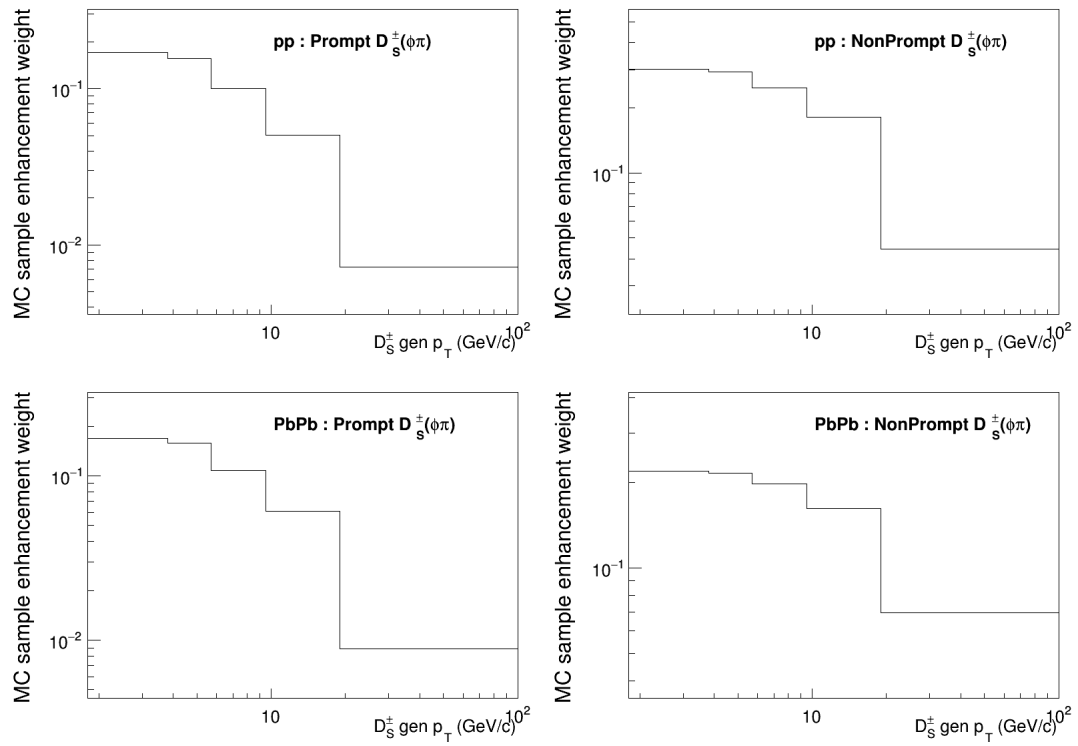


Figure 3.1. MC sample enhancement weight v.s. $D_s^\pm p_T$

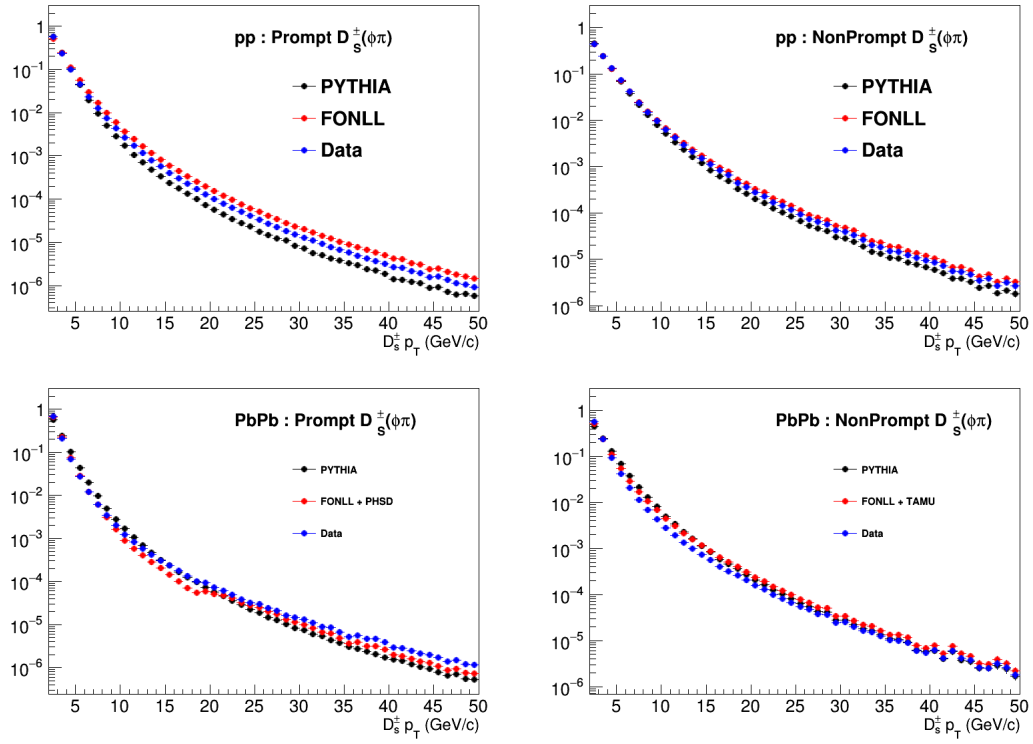


Figure 3.2. Weighted MC D_s^+ p_T distributions

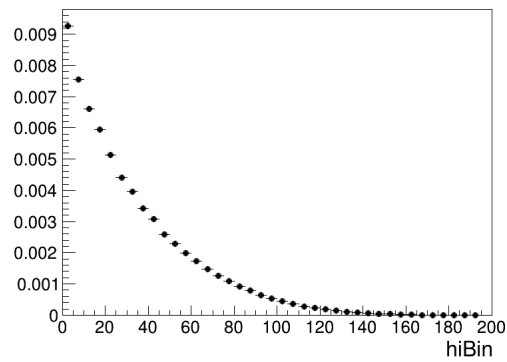


Figure 3.3. Weighted PbPb MC D_s^+ p_T distributions v.s hiBin.

3.3.2 MC D_s^+ Decay Length Tuning

The D_s^+ decay vertex is fitted by three charged tracks ($K^+K^-\pi^\pm$) in this analysis (see chapter 4.1 for details). It is observed that the detector performance is different in Data and MC (Fig. 3.4 left), in which the Data part is obtained by taking the distribution in D_s^+ signal region (D_s^+ mass mean $\pm 2\sigma$), then subtracting the distribution in the sideband region ($> 3\sigma$ from D_s^+ mass mean) according to the fraction of background in the signal region.

To minimize the effect in efficiency from resolution difference between data and MC sample, an extra tuning is applied to the MC sample to better match with data: an scale (scanned with scale ranged from 0.5 to 2) is applied on both prompt and nonprompt MC simultaneously, and the best scale is determined by minimizing the χ^2 . Figure 3.4 shows the decay length error distribution for MC and data, before (left) and after applying scale (right). The best scales are shown in Fig. 3.5. Accordingly, the decay length is smeared with an extra factor : $\text{Decay Length Error} \times \sqrt{1 - (1/\text{scale})^2}$. The systematic uncertainties imposed by this tuning is estimated by comparing the results of using best scale with the result of using scale equals to best scale $\pm 1\sigma$.

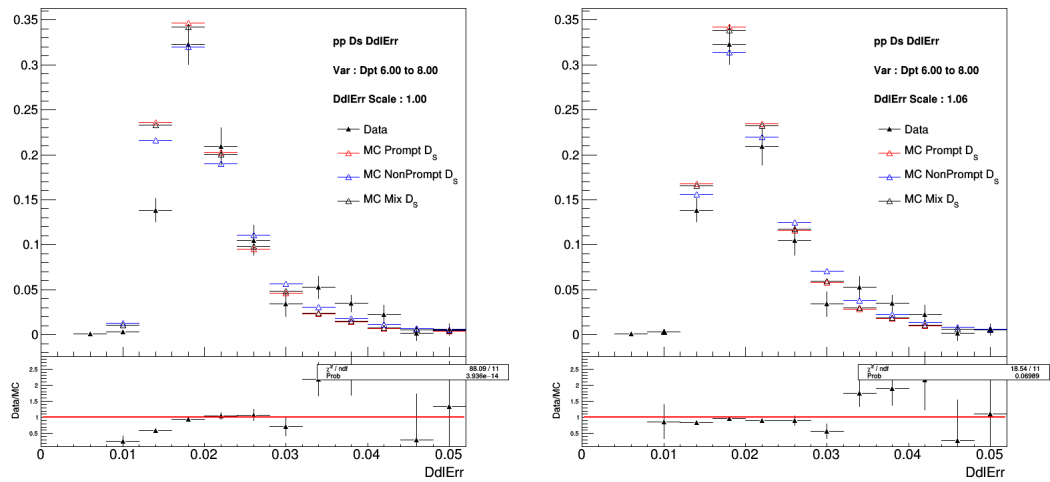


Figure 3.4. Comparison of D_s^+ decay length error distribution of Data and MC. The left panel is with no MC scale. The right panel is with the best MC scale.

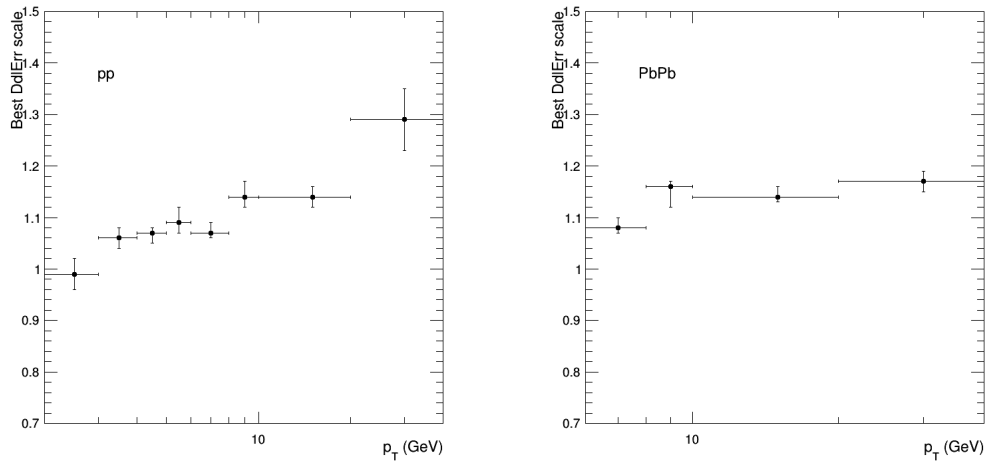


Figure 3.5. The best MC decay length error scale in pp (left) and PbPb (right), the error is estimated by taking the scale with $\chi^2 = \chi_{Best}^2 + 1$.

4. D_S^\pm RECONSTRUCTION AND SIGNAL EXTRACTION

In this chapter, the reconstruction of D_s^\pm candidate with selection optimization and signal extraction is described.

4.1 D_S^\pm Reconstruction

D_s^\pm candidates are reconstructed through the $D_s^+ \rightarrow \phi\pi^+ \rightarrow K^+K^-\pi^+$ decay channel by picking all possible combinations of two opposite charged tracks pair and one charged track in each event. The two opposite charged tracks are assumed to be a kaon pair(the kaon mass is assigned to these two tracks) and having the invariant mass within 9 MeV from the nominal ϕ mass (1019.461 MeV) from particle data group (PDG) (46), while the other track is assumed to be a charged pion with pion mass assigned. The tracks used in reconstruction must fulfill the selection listed in Table 4.1. The D_s^+ decay vertex (secondary vertex) is fitted by using "Kinematic-ParticleVertexFitter"(47; 48), which is an vertex fitter with its algorithm based on least-means-squared minimization with Lagrange multipliers for physics constraints. To reduce combinatorial background, several selections on topological properties are applied :

- three-dimensional displacement from primary vertex to decay vertex normalized to its error (d_0/σ_{d_0} , decay length significance)
- pointing angle (α), the angle between the vector of decay length and the vector of total momentum of the tracks.
- the secondary vertex probability, which is computed by the three tracks reconstruction vertex fitting χ^2 with the number of degrees of freedom of the fit.

Details of selection are described in Section 4.2.

Table 4.1.
Track selection criteria for pp and PbPb events.

	Track quality	$ \eta $	p_T	trkPtError/trkPt
pp	highpurity	< 1.5	> 0.7	< 0.3
PbPb	highpurity	< 1.5	> 1.0	< 0.3

4.2 Selection Cut Optimization

In order to observe the signal with a better statistical significance, the Toolkit for Multivariate Data Analysis with ROOT (TMVA) package (49) is used with rectangular cut method to optimize selection cuts. The optimization criteria for TMVA is determined based on the statistical significance defined as $S/\sqrt{S+B}$, within the signal region, which is defined as $\pm 2\sigma$ (the width of D_s^+ candidate mass in data $0.01 \text{ GeV}/c^2$) from mass of D_s^+ from the PDG. Here, S is the expected number of signals, estimated by D_s^+ cross-section multiplied by efficiency with optimal cuts, while B is the expected number of background, estimated by sideband ($1.91 \text{ GeV}/c^2$ to $1.93 \text{ GeV}/c^2$ and $2.01 \text{ GeV}/c^2$ to $2.03 \text{ GeV}/c^2$, which is outside the 3σ of D_s^+ mass) of data with the optimal cut efficiency and normalized to the width of the signal region. For TMVA training, reconstructed D_s^+ candidates which match with generated D_s^+ particles in MC are used as signal sample, while sideband is used as background. Both signal and background samples are applied with the following initial cuts to reduce the size of the data:

- decay length significance (d_0/σ_{d_0}) > 1.5 for pp and > 2.5 for PbPb
- pointing angle (α) < 0.12
- the secondary vertex probability > 0.02 for pp and > 0.05 for PbPb
- ϕ mass window $< 9 \text{ MeV}/c^2$

Two topological variables are used for training and optimization: decay length significance (d_0/σ_{d_0}) and the secondary vertex probability, while the pointing angle (α) is fixed to less than 0.12. Figures 4.1 and 4.2 show the significance versus the relative signal efficiency (with respect to the initial cuts), with the vertical indicate the optimized cut.

The result of optimized selection are summarized in Table 4.2

Table 4.2.
Summary table of the selection criteria in different p_T intervals.

p_T (GeV/c)	α	Vertex Probability	$d_0/\sigma(d_0)$
pp collisions			
2-3	< 0.12	> 0.19	> 3.70
3-4	< 0.12	> 0.10	> 3.32
4-5	< 0.12	> 0.11	> 3.10
5-6	< 0.12	> 0.10	> 2.98
6-8	< 0.12	> 0.05	> 2.83
8-10	< 0.12	> 0.02	> 2.53
10-20	< 0.12	> 0.02	> 2.54
20-40	< 0.12	> 0.02	> 2.69
PbPb collisions			
6-8	< 0.12	> 0.32	> 4.85
8-10	< 0.12	> 0.38	> 6.01
10-20	< 0.12	> 0.15	> 4.70
20-40	< 0.12	> 0.05	> 3.28

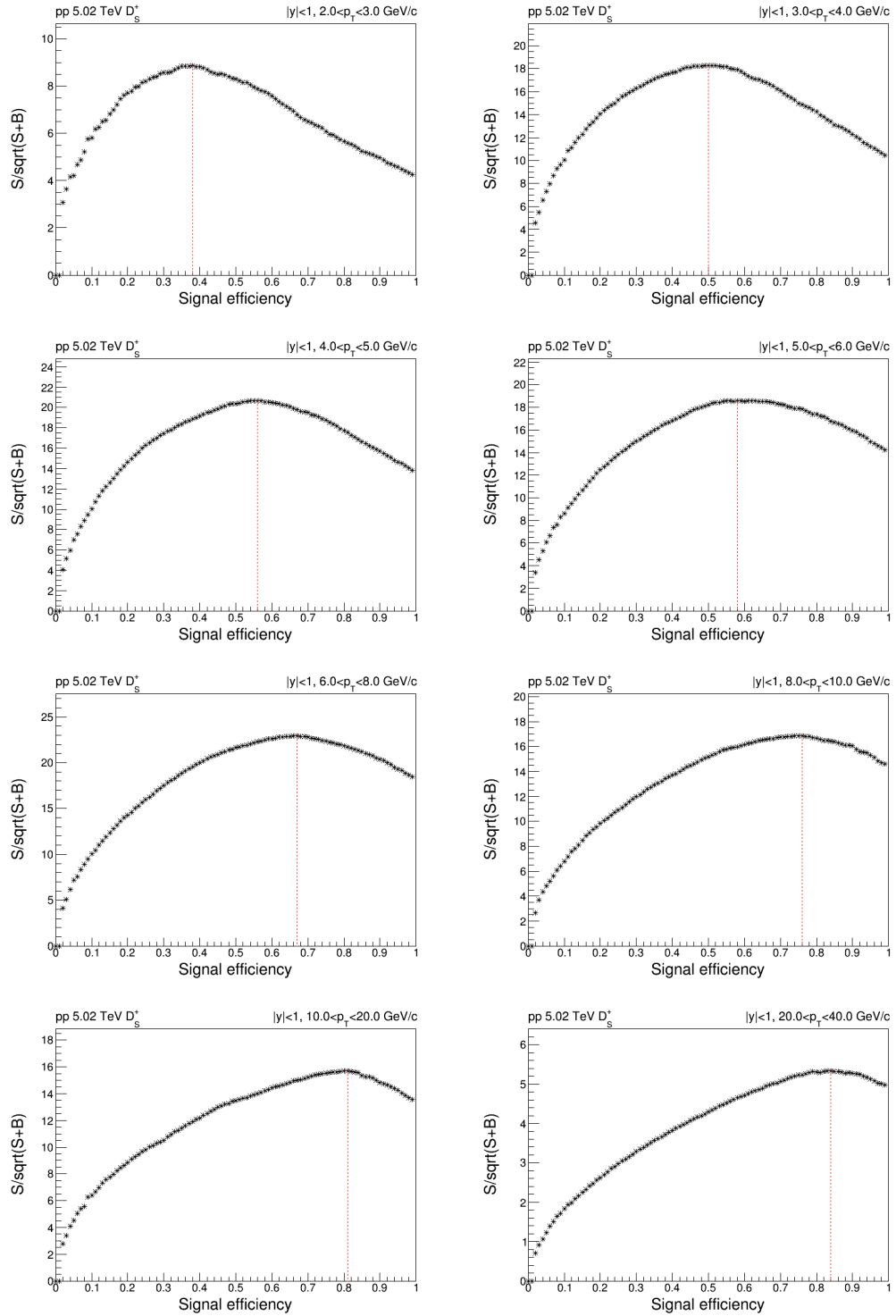


Figure 4.1. Statistical significance $S/\sqrt{S+B}$ versus signal efficiency for pp collision events. Vertical lines indicate the optimized cut.

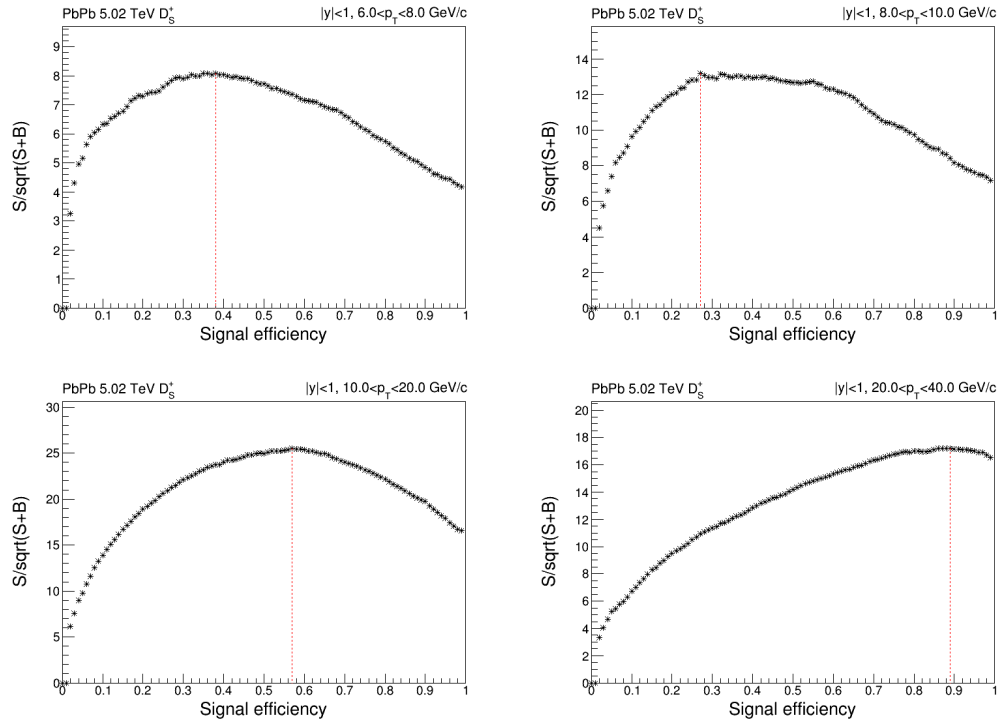


Figure 4.2. Statistical significance $S/\sqrt{S+B}$ versus signal efficiency for PbPb collision events. Vertical lines indicate the optimized cut.

4.3 Signal Extraction

One dimensional unbinned fitting procedure with the package ROOFIT(50) is used to extract D_s^+ signals from D_s^+ candidates in each p_T intervals to the invariant mass of $K^+K^-\pi^\pm$. Based on the MC study shown in Fig. 4.3, there are some contributions of D_s^+ signals from the $f_0(\rightarrow K^+K^-)\pi$ channel after applying the ϕ mass window selection. The shape of $KK\pi$ invariant mass in this channel resembles the shape of D_s^+ from the $\phi(\rightarrow K^+K^-)\pi$ channel since for both channels the mass of daughter tracks are correctly assigned. In the signal extraction and the cross-section calculation, the contribution from $f_0(\rightarrow K^+K^-)\pi$ channel would be included as a source of signal in addition to the $\phi(\rightarrow K^+K^-)\pi$ channel. On the other hand, the contributions from \overline{K}^*K^+ and for those D_s^+ reconstructed with correct track collection but with wrong mass assignment (e.g. swap one of the kaon with pion mass assignment) are small and will be absorbed in the combinatorial background fitting function.

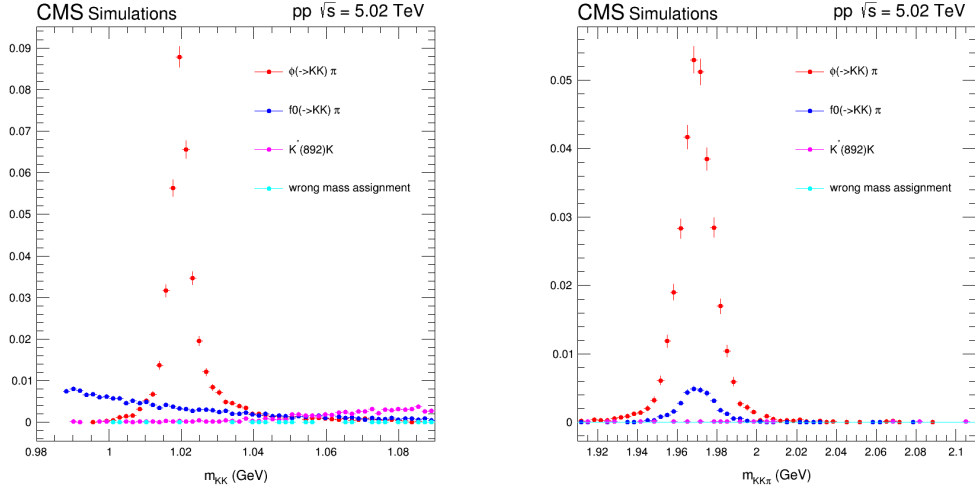


Figure 4.3. The mass distribution of D_s^+ to : $\phi(\rightarrow K^+K^-)\pi^+$, $f_0(\rightarrow K^+K^-\pi^+)$, $\overline{K}^*(\rightarrow K^-\pi^+)K^+$ with generated-matched signal and the D_s^+ signal with correct track collection but wrong mass assignment. *Left* : Invariant mass of K^+K^- pair. *Right* : Invariant mass of $K^+K^-\pi^+$, with the ϕ mass window selection applied.

The fit function consists of two components:

- Signal: double Gaussian with identical means but different widths (σ_1, σ_2) and fraction ($fr_1, (1 - fr_1)$).
- Background : first/second order Chebyshev polynomials.

and could be expressed as :

$$n_{sig} \times (fr_1 \times Gaus_1(mean, [1+(floatwidth)] \times \sigma_1) + (1 - fr_1) \times Gaus_2(mean, [1+(floatwidth)] \times \sigma_2)) + Chebshevpolynomials \quad (4.1)$$

The shape of the double Gaussian is first determined by the signal MC as shown in Fig. 4.4. The relative ratio of width and area of the two Gaussian will remain fixed when fitting data, while the mean and an overall scale (floatwidth) applied on width of both Gaussian are left to float to accommodate the discrepancy between MC and data. All parameters of the background function are left to float in the fit. First-order Chebyshev polynomials are used for background except using second order in PbPb p_T 6-8 and 8-10 GeV/c bins, based on likelihood ratio test result. The D_s^+ raw yield fitting results are shown in Fig. figs. 4.5 to 4.7.

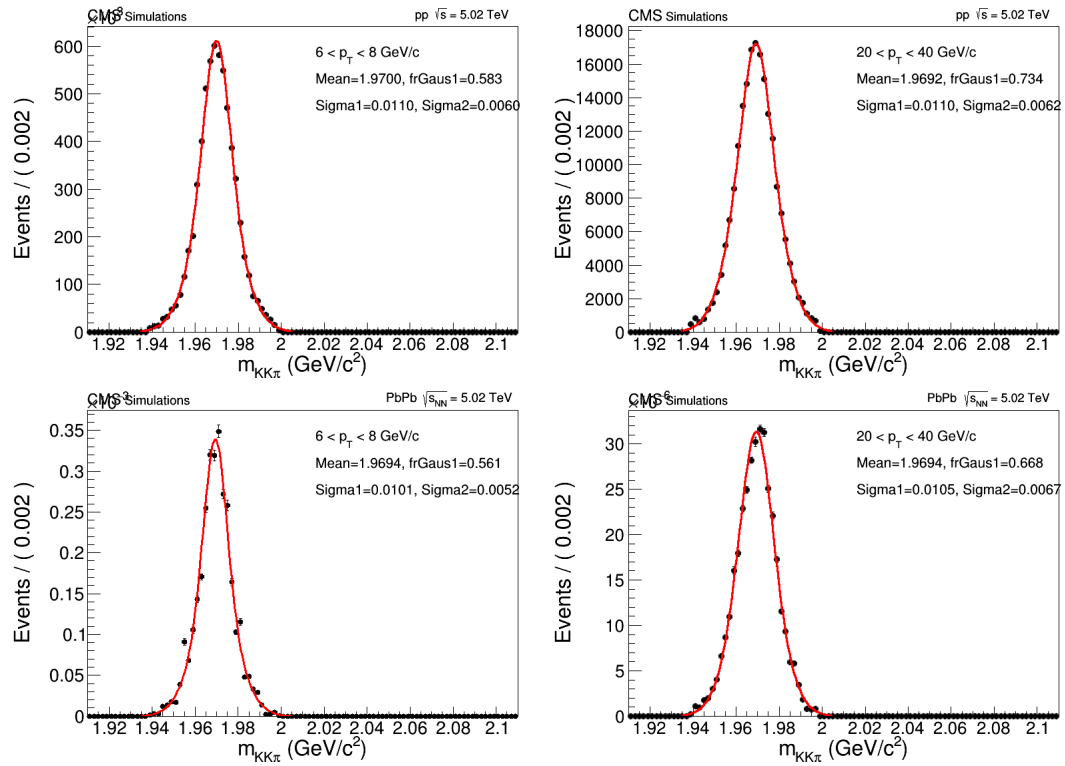


Figure 4.4. Double Gaussian fit for pp (top) and PbPb (bottom) signal MC in $p_T = 6 - 8$ (left) and $20 - 40$ GeV (right).

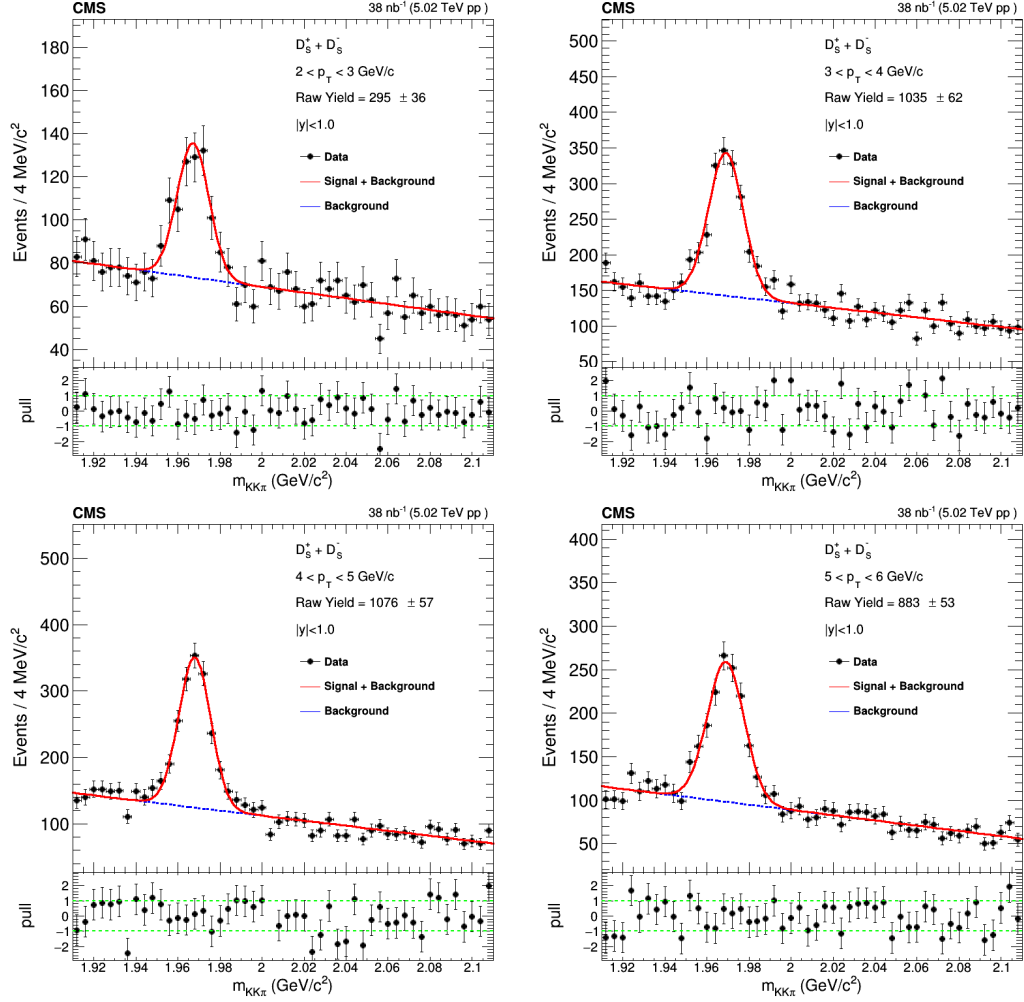


Figure 4.5. Invariant mass distribution of D_s^+ candidates with p_T from 2 to 6 GeV/c in pp collisions at $\sqrt{s} = 5.02$ TeV with signal extraction fitting curve. The blue dashed line represents the background fit, while the red solide line represents the signal plus the background fit.

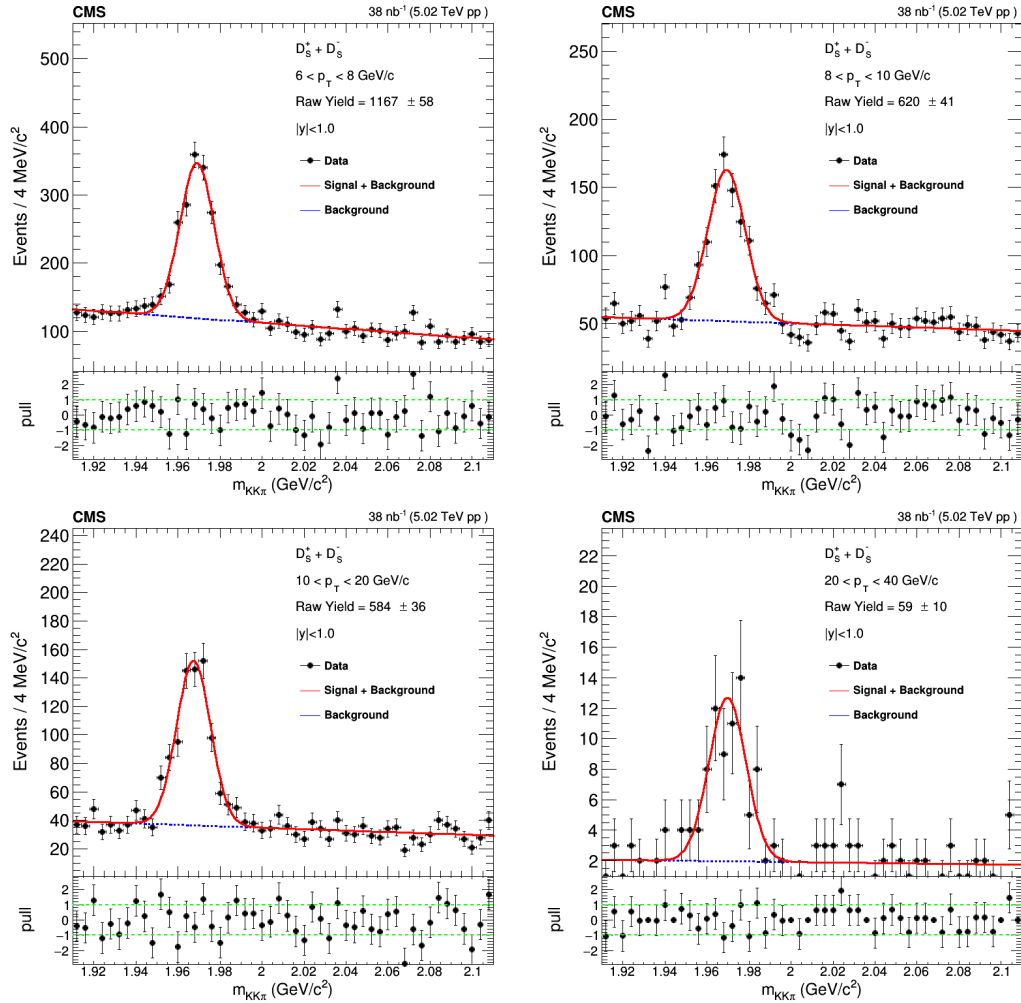


Figure 4.6. Invariant mass distribution of D_s^+ candidates with p_T from 6 to 8 GeV/c in pp collisions at $\sqrt{s} = 5.02$ TeV with signal extraction fitting curve. The blue dashed line represents the background fit, while the red solid line represents the signal plus the background fit.

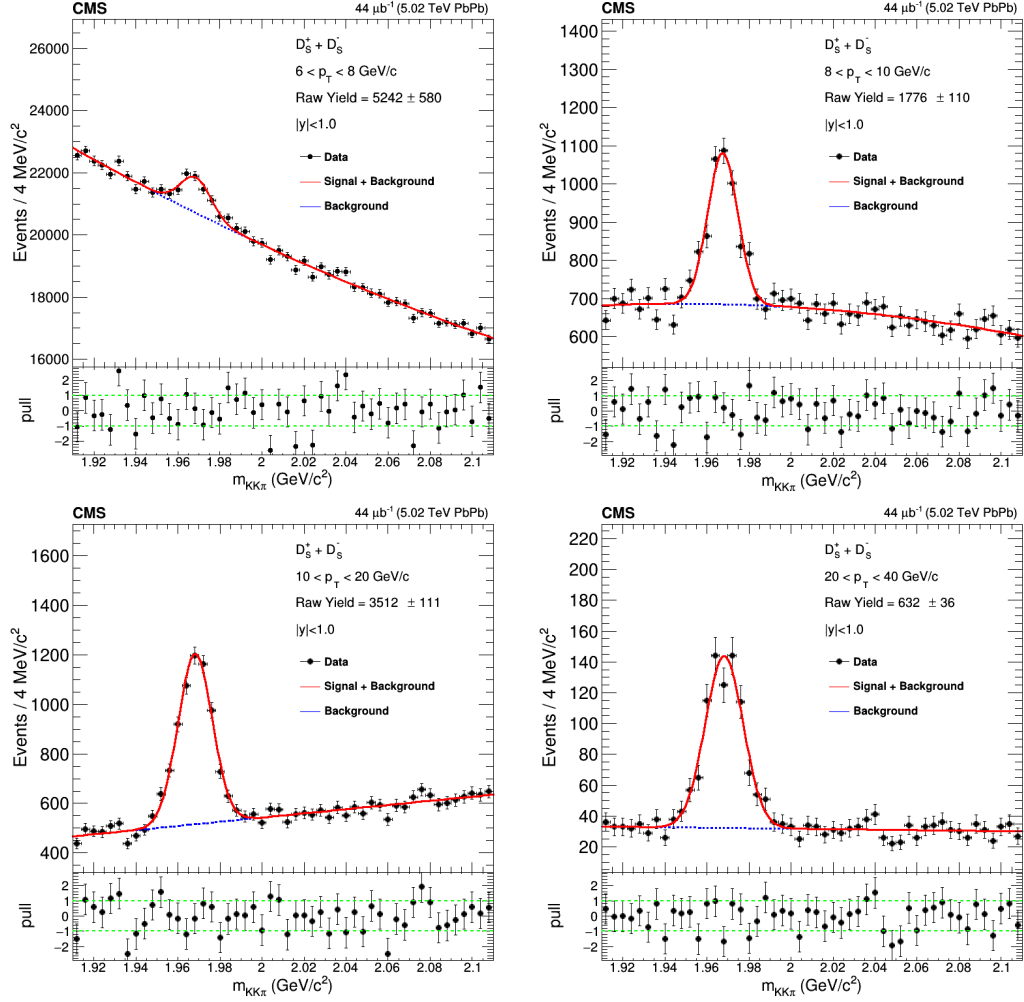


Figure 4.7. Invariant mass distribution of D_s^+ candidates with p_T from 6 to 8 GeV/c in PbPb collisions at $\sqrt{s_{NN}} = 5.02$ TeV with signal extraction fitting curve. The blue dashed line represents the background fit, while the red solid line represents the signal plus the background fit.

4.4 $D_s^\pm \rightarrow \phi\pi^\pm$ Channel Ratio Extraction

MC studies shown in Fig. 4.3 indicate that there are other sources to the yield extracted in sec. 4.3 in addition to $D_s^+ \rightarrow \phi\pi^\pm$ channel. A data-driven method is used to extract this ratio ($D_s^+ \rightarrow \phi\pi^\pm \rightarrow K^+K^-\pi^\pm$ channel over all $D_s^+ (\rightarrow K^+K^-\pi^\pm)$). The data is divided into different bins based on the invariant mass of K^+K^- pairs. In each bin, the D_s^+ yield is extracted using the nominal fitting procedure. Collecting all fitting results from different $m_{K^+K^-}$ bins, then fitted with triple CrystalBall function, all parameters are the same except sigma, for signal, and first-order polynomial for backgrounds, as shown in Fig. 4.8 and 4.9. $\phi\pi$ channel ratio is obtained by taking the signal yield over total yield ratio within analysis ϕ mass window selection.

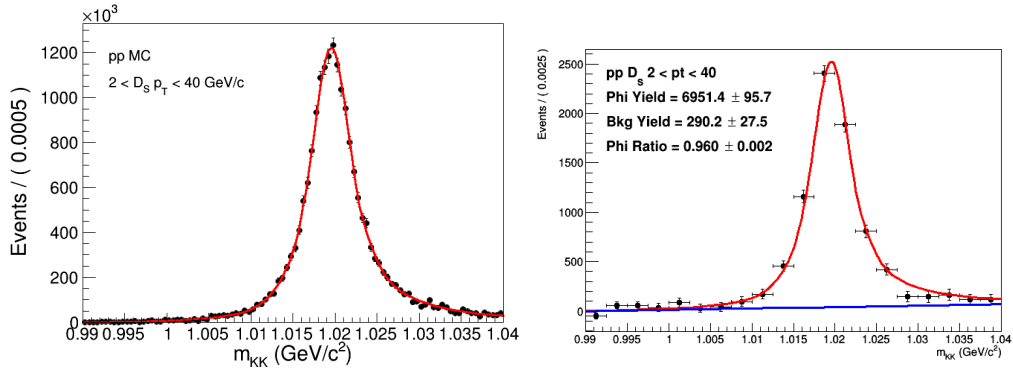


Figure 4.8. Fitting plot of invariant mass of K^+K^- in pp. *Left*: MC. *Right*: data.

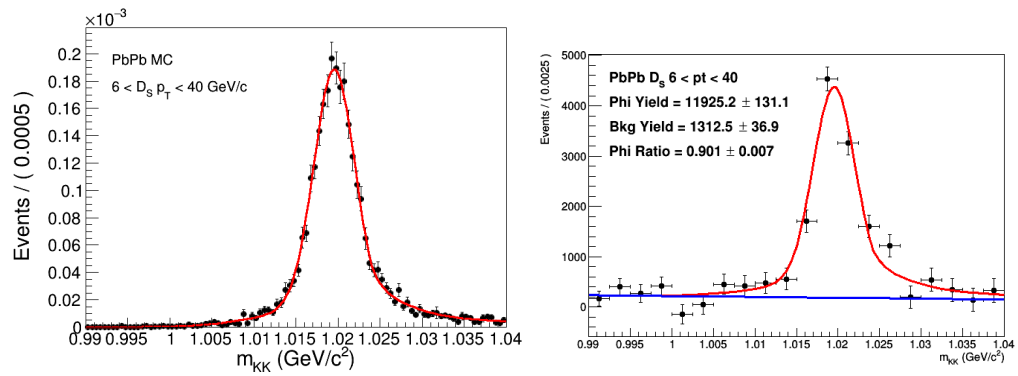


Figure 4.9. Fitting plot of invariant mass of K^+K^- in PbPb. *Left*: MC. *Right*: Data.

4.5 Acceptance and Efficiency Correction

Acceptance and efficiency(ϵ) corrections are applied to the extracted raw D_s^+ yield to get the corrected spectra. The studies are performed with the signal MC sample for pp and PbPb described in Sec. 3.3. The acceptance is defined as the fraction of D_s^+ mesons generated in rapidity range $|y| < 1$ with all of their daughter tracks fulfill the track acceptance selections(track p_T and η selection as listed in Table 4.1). The reconstruction efficiency (ϵ_{Reco}) is defined as the tracks fulfilling the track selections and also be reconstructed. The selection efficiency(ϵ_{sel}) is defined as the fraction of reconstructed D_s^+ fulfilling the optimized selection listed in Table 4.2. Results for pp collisions are shown in Fig. 4.10, and for PbPb collisions are shown in Fig. 4.11.

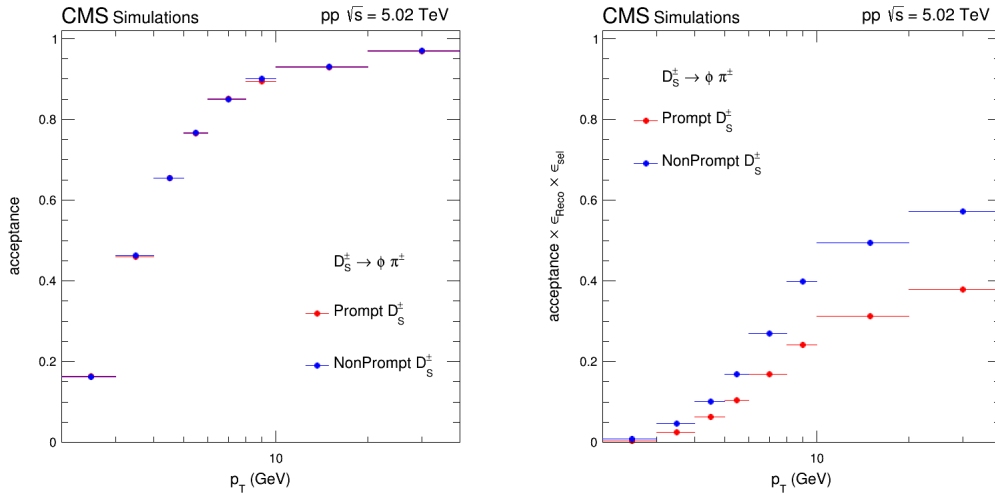


Figure 4.10. Prompt D_s^+ (red) and nonprompt D_s^+ (blue) to $\phi\pi^\pm$ acceptance (left), and acceptance times total efficiency (right) for pp collision at $\sqrt{s} = 5.02$ TeV.

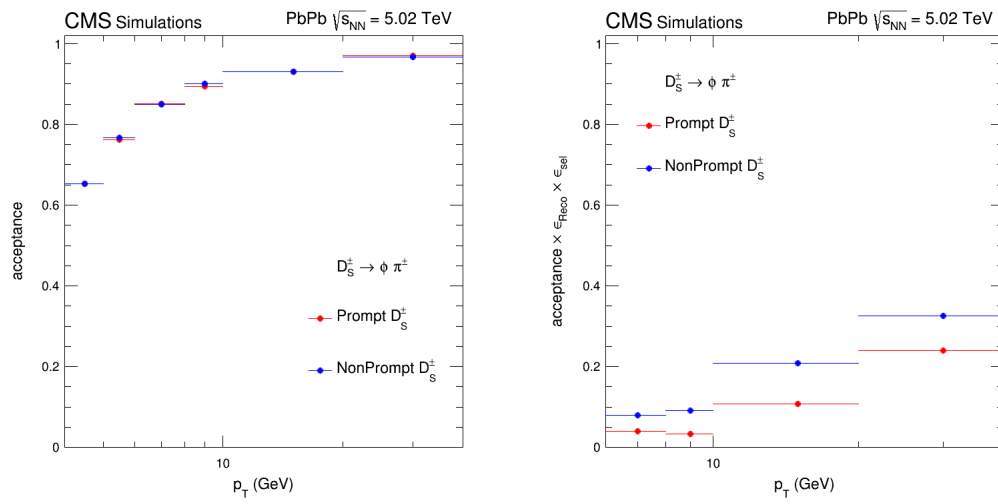


Figure 4.11. Prompt D_s^+ (red) and nonprompt D_s^+ (blue) to $\phi\pi^\pm$ acceptance (left), and acceptance times total efficiency (right) for PbPb collision at $\sqrt{s_{NN}} = 5.02$ TeV.

4.6 Nonprompt D_s^\pm Estimation

There are two sources for the D_s^+ raw yield extracted in Chapter 4.3 : prompt and nonprompt D_s^+ (D_s^+ from b hadron decays). In order to obtain the prompt D_s^+ spectra, the number of non-prompt D_s^+ has to be subtracted from the total yield. In this analysis, a semi-data driven method is used to estimate the non-prompt D_s^+ yield.

To estimate non-prompt D_s^+ , the similarity between nonprompt D^0 and non-prompt D_s^+ is exploited. The nonprompt D^0 spectra in pp and PbPb collision at 5.02 TeV have been measured in CMS PAS HIN-16-016 (41). The following two steps are applied to nonprompt D^0 for getting non-prompt D_s^+ spectra by this formula:

$$\frac{d\sigma_{nonprompt}^{D_s^++D_s^-}}{dp_T} = \frac{d\sigma_{nonprompt}^{D^0+\bar{D}^0}}{dp_T} \times \frac{\sum_B fr(B) \times Br(B \rightarrow D_s^+)}{\sum_B fr(B) \times Br(B \rightarrow D^0)} \times \frac{D_s^+ p_T shape}{D^0 p_T shape} \quad (4.2)$$

- D^0 to D_s^+ scale: the summation term in Eq. (4.2). The difference of total cross section of nonprompt D^0 and D_s^+ is determined by two factors : B fragmentation fraction (the fraction of B^+ , B^0 , B_S and b baryons) and the branching ratio of b hadrons to D_s^+ and D^0 . The B in the equation stands for B^+ , B^0 , B_S . The quantity $fr(B)$ is the B fragmentation fraction, for which we use the LHCb result in pp collision at $\sqrt{s} = 7$ TeV (51) as nominal value. $Br(B \rightarrow D_s^+ (or D^0))$ denotes the branching ratio obtained by the PDG (in Table 4.3). The value of D^0 to D_s^+ scale is 0.313, and applying it to the nonprompt D^0 spectra to obtain the total cross section corrected non-prompt D_s^+ spectra. A study based on PYTHIA simulation shows that there is no energy or rapidity dependence of the B meson fractions (see Fig. 4.12).
- D^0 to D_s^+ p_T differential distribution :the last term in Eq. (4.2). The difference of non-prompt D^0 and D_s^+ is considered by comparing the PYTHIA 8 MC distributions. A normalized p_T differential distribution of non-prompt D^0 and D_s^+ is shown in the left panel of Fig. 4.13. The ratios of D^0 and D_s^+ results in

each analysis p_T bin (cf. the right panel of Fig. 4.13) are then applied to the nonprompt D_s^+ spectra obtained in last step.

The estimated results for the nonprompt D_s^+ cross section in pp and dN/dp_T are shown in Fig. 4.14. The prompt fraction, $f_{prompt}^{D_s^+} = \frac{\sigma_{prompt}^{D_s^+}}{\sigma_{prompt}^{D_s^+} + \sigma_{nonprompt}^{D_s^+}}$, is shown in Fig. 4.15, using the cross section of prompt D_s^+ obtained in Chapter 6;

Table 4.3.
Branching ratio of B mesons to D mesons.

Branching ratio	B^0	B^\pm	B_S
D^0	0.555 ± 0.043	0.876 ± 0.047	0.00213 ± 0.00043
D_s^+	0.103 ± 0.021	0.09 ± 0.018	0.93 ± 0.25

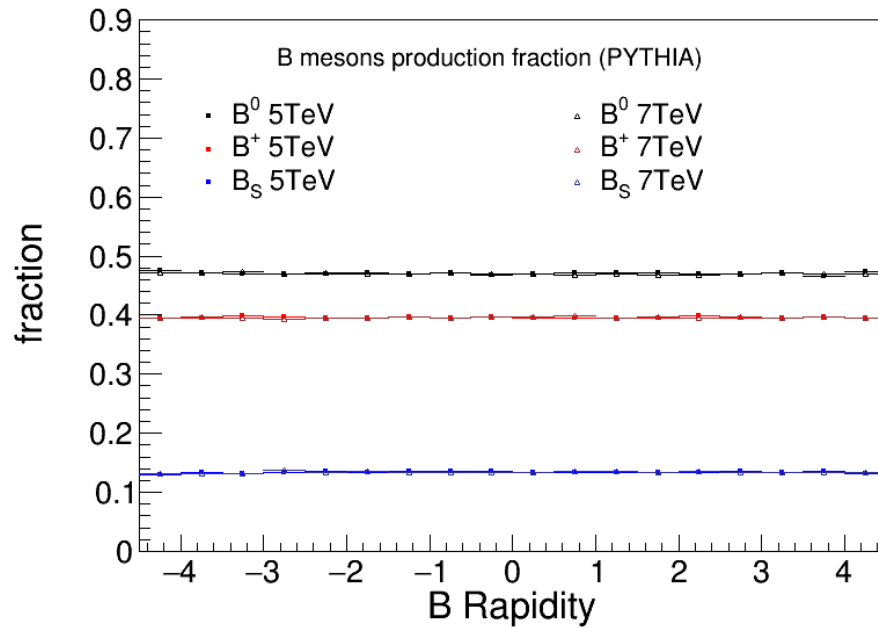


Figure 4.12. B mesons fraction v.s rapidity at different collision energy by PYTHIA simulation.

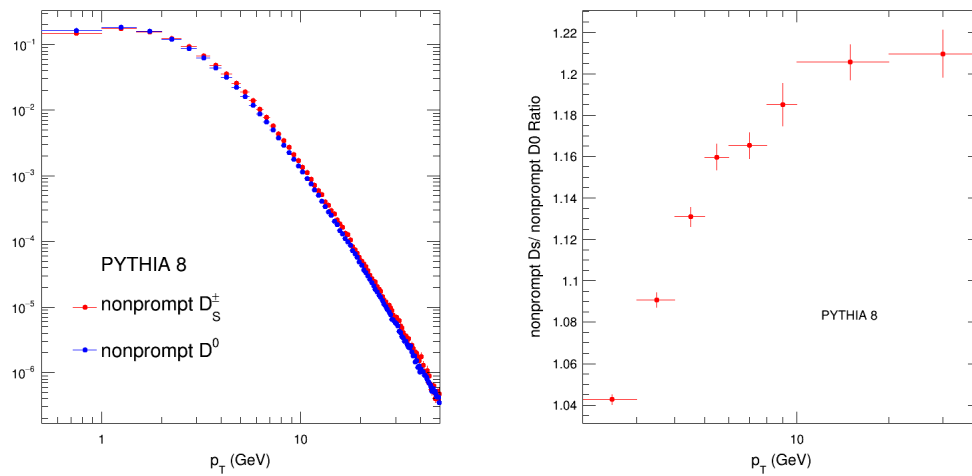


Figure 4.13. *Left* : normalized p_T distribution of nonprompt D_S^+ and D^0 from PYTHIA 8 MC. *Right* : the ratio of nonprompt D_S^+ over nonprompt D^0 in the analysis p_T bins.

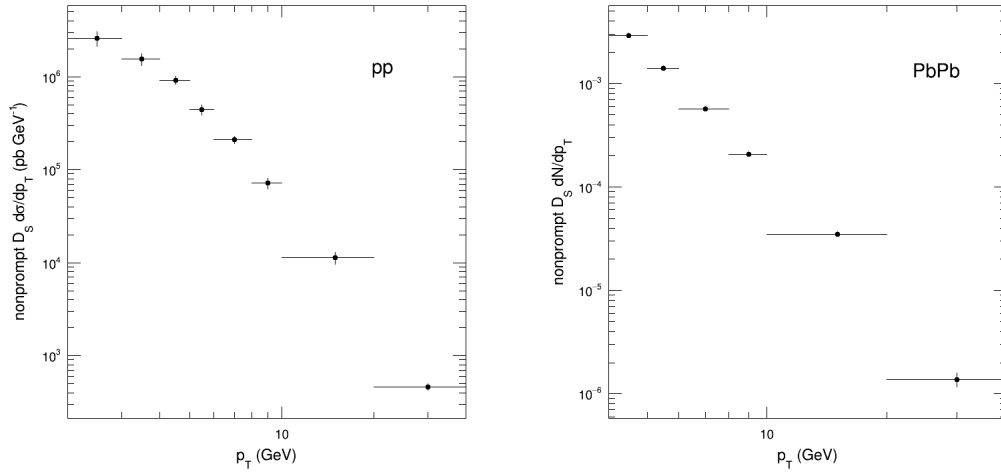


Figure 4.14. Estimated p_T differential cross section of nonprompt D_s^+ in pp collision (left), and dN/dp_T of nonprompt D_s^+ in PbPb collision (right).

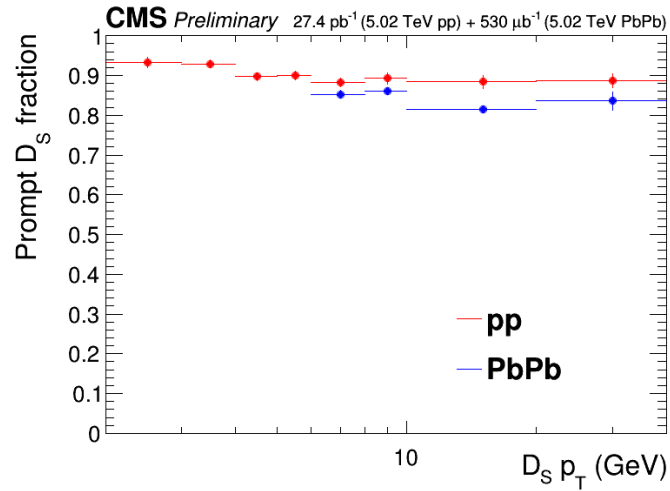


Figure 4.15. Fraction of prompt D_s^+ differential cross sections to all D_s^+ .

5. SYSTEMATIC UNCERTAINTIES

In this chapter, the systematic uncertainties of this analysis are presented. Summaries of systematic uncertainties are shown in Sections 5.1 to 5.4. Details of systematic uncertainties are described in Sections 5.5 to 5.8.

5.1 Summary of Systematic Uncertainties on the Proton-Proton Cross Section

The D_s^+ cross sections in pp collisions are affected by several sources of systematic uncertainties listed in Table 5.1. The uncertainty of tracking efficiency is estimated by using the result of CMS PAS HIN-16-001 (52), based on which the single track uncertainty is 4% in pp and 5% in PbPb collisions. Thus, for the D_s^+ candidate reconstructed from three charged tracks, the tracking uncertainty is 12% in pp and 15% in PbPb collision. The uncertainty in the MC decay length tuning is described in Section 3.3.2. The details of systematic uncertainties associated with selection efficiency (Section 5.5), signal extraction (Section 5.6), MC p_T shape (Section 5.7) and nonprompt Ds (Section 5.8) are discussed in each section separately. The uncertainty associated with D_s^+ meson decay branching fraction is 3.5% according to the Particle Data Group. The total systematic uncertainty in each p_T interval is the quadrature sum of each individual term above. The sources of global uncertainty from the luminosity for pp, which is 2.3% based on study on the VdM scan data (53), is listed separately.

Table 5.1.
Summary of relative systematics (%) for 5.02 TeV pp collisions.

Source	p_T interval (GeV)							
	2-3	3-4	4-5	5-6	6-8	8-10	10-20	20-40
Tracking efficiency	12							
Selection efficiency	7.9	4.6	7.3	8.5	2.5	2.6	3.5	2.8
Signal extraction	0.1	0.4	1.0	0.2	0.3	0.4	0.0	1.9
MC p_T shape	1.6	0.6	0.3	0.1	0.2	0.0	0.0	0.1
MC decay length tune	4.9	2.4	1.8	2.8	1.5	1.7	1.1	2.4
Nonprompt D_s^+	5.1	4.4	6.2	5.2	5.7	5.6	6.6	5.1
Branching ratio	3.5							
Total bin by bin	16.5	14.3	15.9	16.2	14.0	14.1	14.6	14.1
Luminosity	2.3							

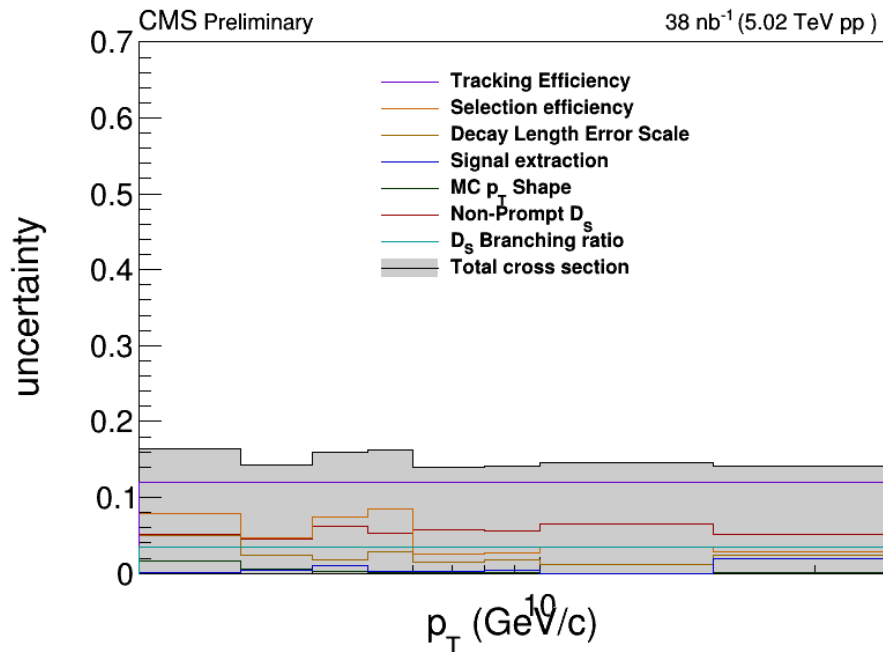


Figure 5.1. Summary of relative systematics (%) for 5.02 TeV pp collisions.

5.2 Summary of Systematic Uncertainties on the PbPb dN/dp_T

The systematic uncertainties in PbPb are arising from the selection efficiency, signal extraction, MC p_T shape and non-prompt D_s^+ are evaluated by the same method as in the proton-proton analysis (Sections 5.5 to 5.8). The hadron tracking systematics in PbPb collision is quoted from the D^0 study, 5% per track, thus 15% in total. The total systematic uncertainty in each p_T interval is the quadrature sum of each individual term above. The global systematic uncertainty on the determination of the numbers of events is affected by 2%, based on the studies done with HF energy spectra from the CMS heavy-ion centrality group. The result is shown in Table 5.2.

Table 5.2.
Summary of relative systematics (%) for 5.02 TeV PbPb collisions.

Source	p_T interval (GeV)			
	6-8	8-10	10-20	20-40
Tracking efficiency	15			
Selection efficiency	10.0	8.8	4.8	4.3
Signal extraction	2.9	2.3	0.4	0.2
MC p_T shape	0.0	0.3	1.1	0.3
MC Decay Length Tune	3.9	6.9	2.6	1.2
$D_s^+ \rightarrow \phi \pi^\pm$ ratio	1.2			
Nonprompt D_s^+	10.3	13.4	11.8	8.9
Branching ratio	3.5			
Total bin by bin	21.6	23.4	20.2	18.3
Luminosity	2.0			

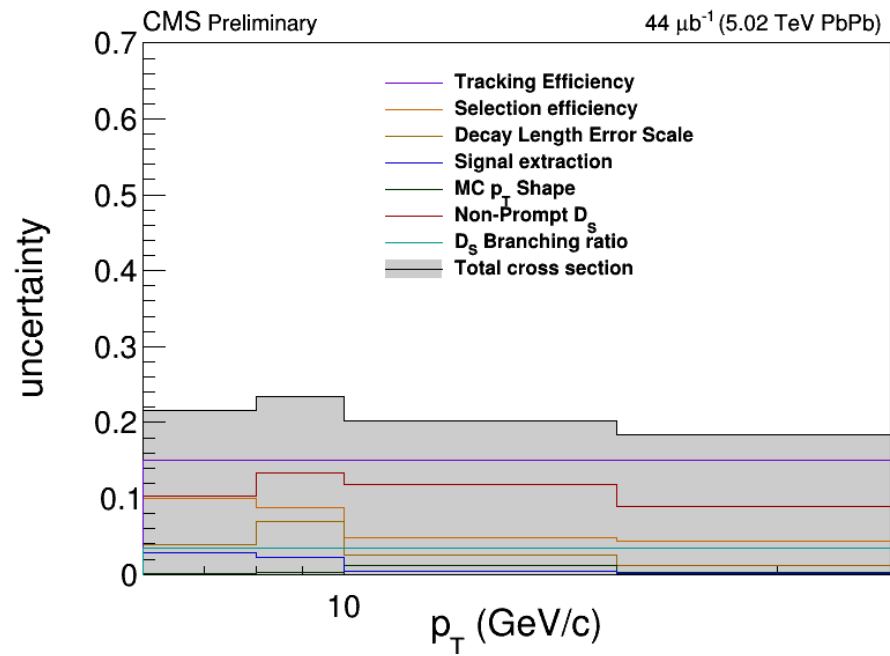


Figure 5.2. Summary of relative systematics (%) for 5.02 TeV PbPb collisions.

5.3 Summary of Systematic Uncertainties on the Nuclear Modification Factor

The systematic uncertainties on the nuclear modification factor inherit the uncertainties in cross section of pp and PbPb (Sections 5.1 and 5.2) and combined with T_{AA} uncertainties from Glauber model calculations. The total systematic are added in quadrature except for the following sources : the branching fraction of D_s^+ , which is canceled when taking the ratio; the systematic for Nonprompt D_s^+ for pp and PbPb in the calculation of total cross section from uncertainties in branching ratio; and B meson fraction are arising from the same sources in pp and PbPb also cancels in the ratio.

Table 5.3.
Summary of relative systematics (%) for the nuclear modification factor in pp and PbPb collisions at $\sqrt{s_{NN}} = 5$ TeV

Source	p_T interval (GeV/c)			
	6-8	8-10	10-20	20-40
Tracking efficiency	18			
Selection efficiency	10.3	9.2	5.9	5.1
Signal extraction	2.9	2.3	0.4	1.9
MC p_T shape	0.2	0.3	1.1	0.3
MC Decay Lenth Tune	4.2	7.1	2.8	2.7
Nonprompt D_s^+	9.9	13.2	12.0	8.4
Total bin by bin	23.5	25.3	22.6	20.8
Luminosity	3.0			
T_{AA}	+2.8, -3.4			

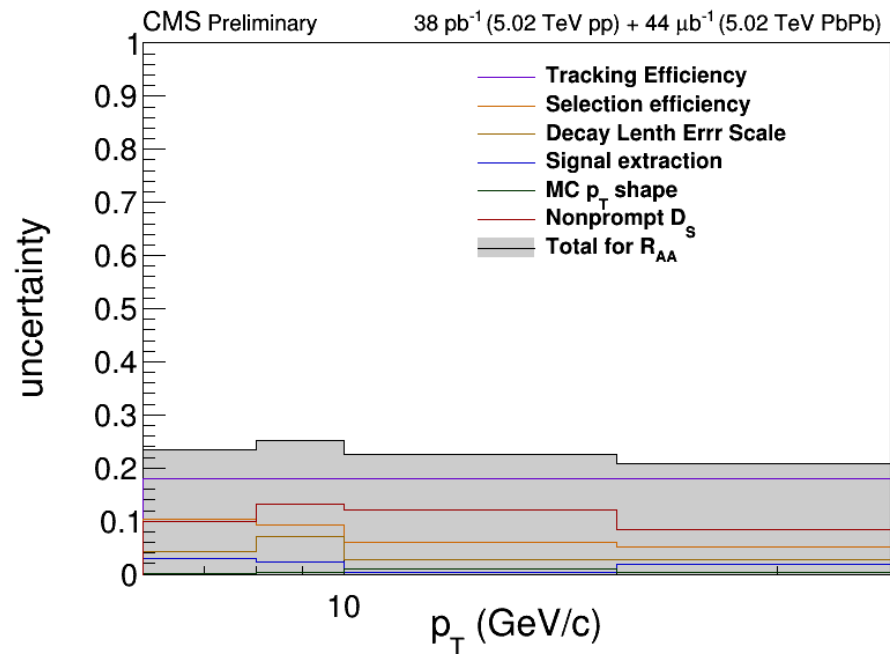


Figure 5.3. Summary of relative systematics (%) for nuclear modification collisions.

5.4 Summary of Systematic Uncertainties on the Ratio of D_s^+ over D^0

The systematics of the ratio of D_s^+ over D^0 are inherited by all the systematics in D_s^+ and D^0 , except the global uncertainty, Luminosity for pp and number of events in PbPb cancels in the ratio. The result is shown in Table 5.4 and Table 5.5.

Table 5.4.

Summary of relative systematics (%) for D_s^+ over D^0 ratio in pp collisions at $\sqrt{s} = 5.02$ TeV.

Source	p_T interval (GeV)							
	2-3	3-4	4-5	5-6	6-8	8-10	10-20	20-40
Tracking efficiency	4							
Selection efficiency D_s^+	7.9	4.6	7.3	8.5	2.5	2.6	3.5	2.8
Selection efficiency D^0	3.6							
Signal extraction D_s^+	0.1	0.4	1.0	0.2	0.3	0.4	0.0	1.9
Signal extraction D^0	8.2	7.6	3.5	3.0	3.0	1.7	4.0	2.3
MC p_T shape D_s^+	1.6	0.6	0.3	0.1	0.2	0.0	0.0	0.1
MC p_T shape D^0	5.0	3.0	2.0	2.0	1.0	1.0	1.0	0.0
MC Decay Length Tune	4.9	2.4	1.8	2.8	1.5	1.7	1.1	2.4
Nonprompt D_s^+	5.1	4.4	6.2	5.2	5.7	5.6	6.6	5.1
Nonprompt D^0	10.0							
Branching ratio D_s^+	3.5							
Branching ratio D^0	1.3							
Total bin by bin	18.7	16.0	16.0	16.2	13.9	13.7	14.7	13.8

Table 5.5.

Summary of relative systematics (%) for D_s^+ over D^0 ratio in PbPb collisions at $\sqrt{s_{NN}} = 5.02$ TeV

Source	p_T interval (GeV)			
	6-8	8-10	10-20	20-40
Tracking efficiency	5			
Selection efficiency D_s^+	10.0	8.8	4.8	4.3
Selection efficiency D^0	3.5			
Signal extraction D_s^+	2.9	2.3	0.4	0.2
Signal extraction D^0	1.7	1.3	6.5	9.4
MC p_T shape D_s^+	0.0	0.3	1.1	0.3
MC p_T shape D^0	5.0	3.0	1.9	0.3
MC Decay Length Tune	3.9	6.9	2.6	1.2
Nonprompt D_s^+	10.3	13.4	11.8	8.9
Nonprompt D^0	10.0			
Branching ratio D_s^+	3.5			
Branching ratio D^0	1.3			
Total bin by bin	20.2	21.7	19.1	18.4

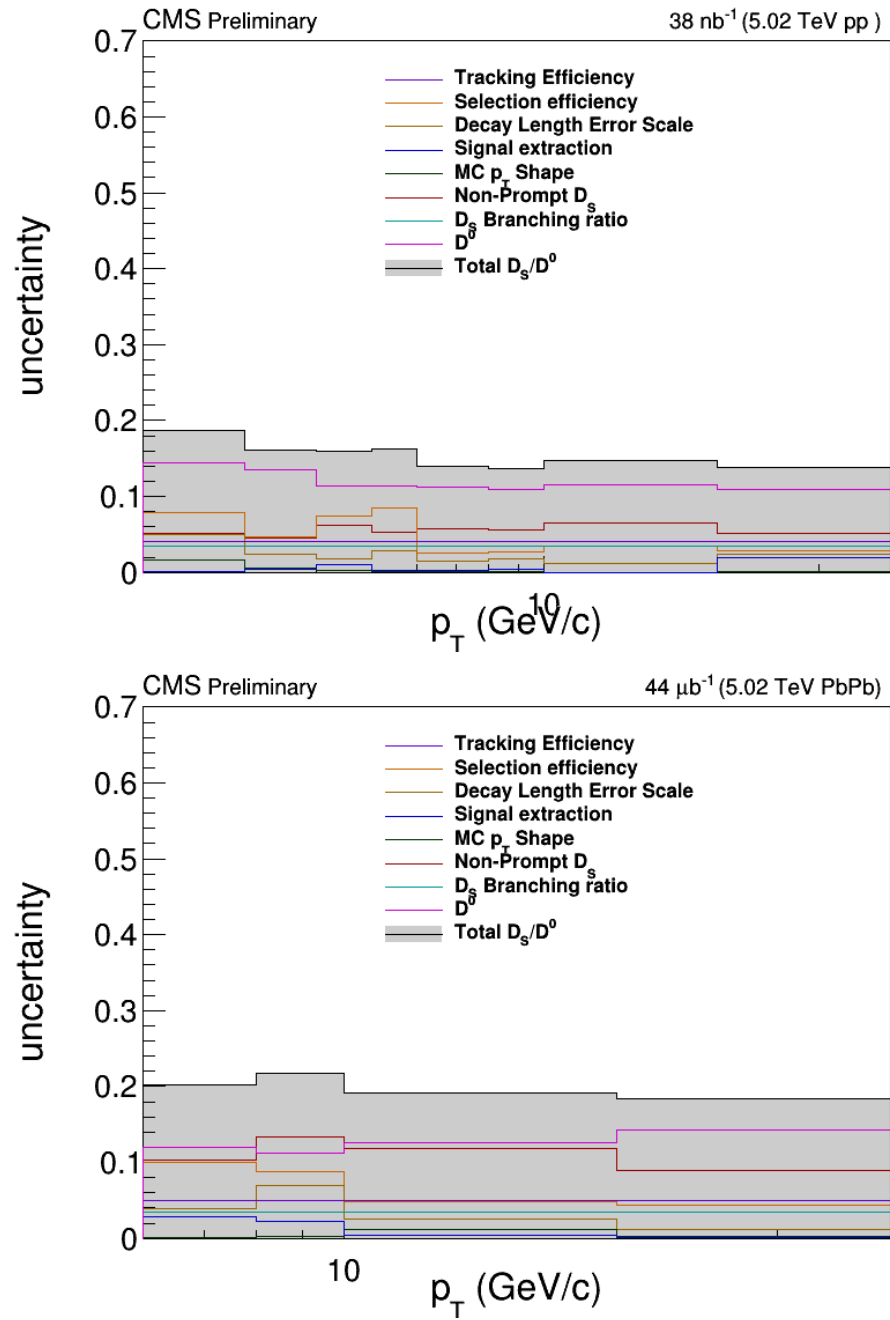


Figure 5.4. Summary of relative systematics (%) for D_s^+ over D^0 ratio in pp and PbPb collisions.

5.5 Systematics Associated with Selection Efficiency

Any discrepancy in a selection variable distribution between D_s^+ MC simulation and D_s^+ signal in data could introduce a bias on the signal efficiency corrections. To evaluate this effect, the following ratio is computed for the selection variable (Vertex Probability) i :

$$Ratio(\text{VariedCut}/\text{DefaultCut})(i) = \frac{\frac{d\sigma^i(\text{variedCut})}{dp_T}}{\frac{d\sigma^i(\text{defaultCut})}{dp_T}} \quad (5.1)$$

where the *DefaultCut* is the selection cut used to obtain the nominal result, and *VariedCut* comes from a series of looser and tighter cut than the default one. Ideally by setting the *VariedCut* to no cut gives us the non-bias result. However, due to the low ratio of signal to backgrounds, it is not possible to extract the signal via fitting without any selection cut. Thus, for the vertex probability, the ratio as a function of the different cut threshold is fitted with a straight line, and using the fit extrapolated to no cuts as the systematics. The cut scan ratios are shown in Figures 5.5 to 5.7.

For D_s^+ pointing angle and decay length significance, an alternative weight based on the signal distribution ratio of data to MC is applied. The signal distribution in data is obtained by using the sPlot (54) method, and the MC is obtained by adding prompt and nonprompt MC together according to the prompt fraction in the given p_T -interval. The signal distribution and the ratio of data to MC are shown in Figures 5.8 to 5.11. For PbPb, in the p_T bin 6–8 GeV/ c , the sPlot method failed to produce the D_s^+ point angle distribution in data. Thus, the alternative weight for this bin is set to the weight for PbPb in the p_T bin 8–10 GeV/ c instead. For decay length significance, the weight outside the ranges shown in the Figures 5.10 and 5.11 is obtained by linear extrapolation. For the ϕ mass window, an additional scale on MC width based on the data and MC fitting in Section 4.4 is applied. The difference between default and alternative weight or scale is taken as systematic uncertainty.

The results are summarized in Tables 5.6 and 5.7

Table 5.6.

Summary of relative systematics (%) for selection efficiency in pp collisions.

Source	p_T interval (GeV)							
	2-3	3-4	4-5	5-6	6-8	8-10	10-20	20-40
Pointing angle	4.6	4.4	6.6	7.6	1.8	1.8	0.6	2.3
Vertex probability	6.3	1.2	3.1	3.6	1.1	1.5	3.3	0.1
Decay length significance	0.1	0.1	0.2	0.2	1.2	0.9	0.4	1.5
ϕ mass window	0.5	0.6	0.8	0.9	0.6	0.8	0.8	0.8

Table 5.7.

Summary of relative systematics (%) for selection efficiency in PbPb collisions.

Source	p_T interval (GeV)			
	6-8	8-10	10-20	20-40
Pointing angle	1.8	3.4	1.0	2.0
Vertex probability	9.8	7.6	3.1	2.4
Decay length significance	0.6	2.9	3.4	2.8
ϕ mass window	0.3	0.3	0.6	0.7

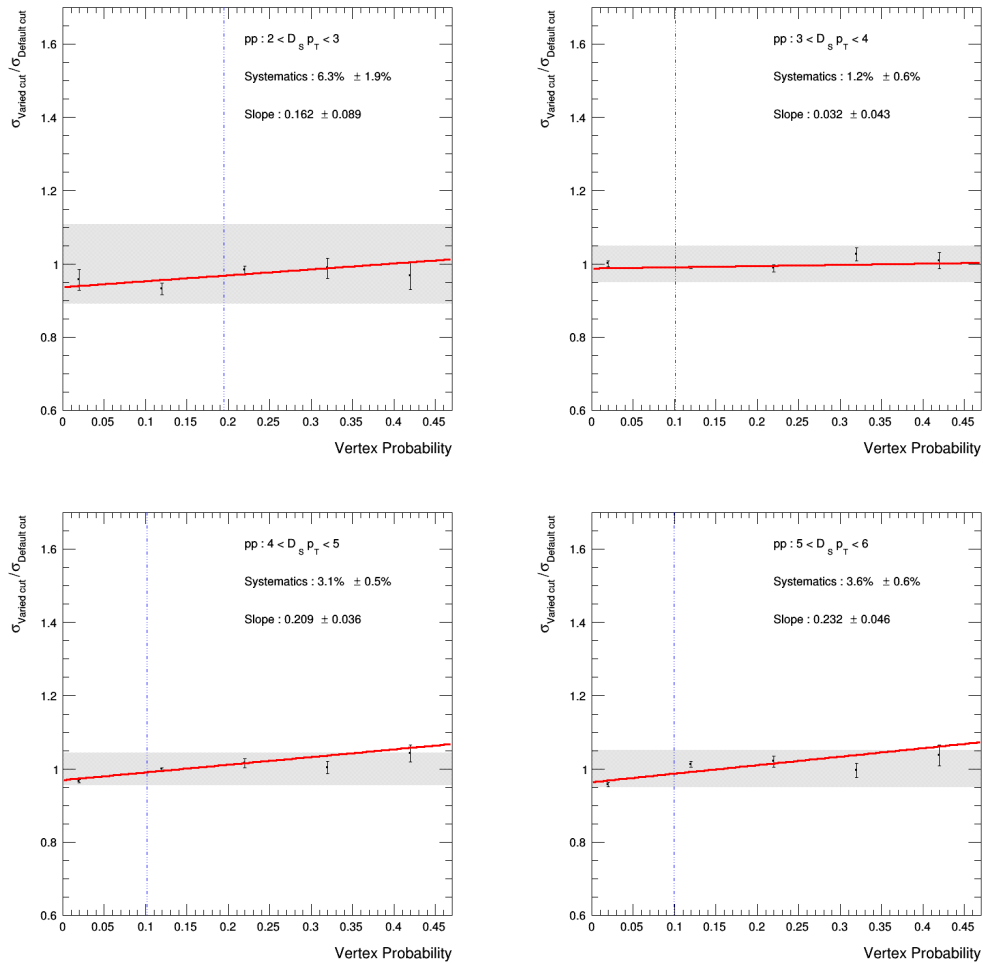


Figure 5.5. Vertex probability scan for D_s^+ with p_T range from 2 to 6 GeV/c in pp collisions, where the y-axis is the cross section ratio of varied cut to default cut. The blue dashed line indicate the default cut used in the analysis. The red dashed line is the linear fit of the data.

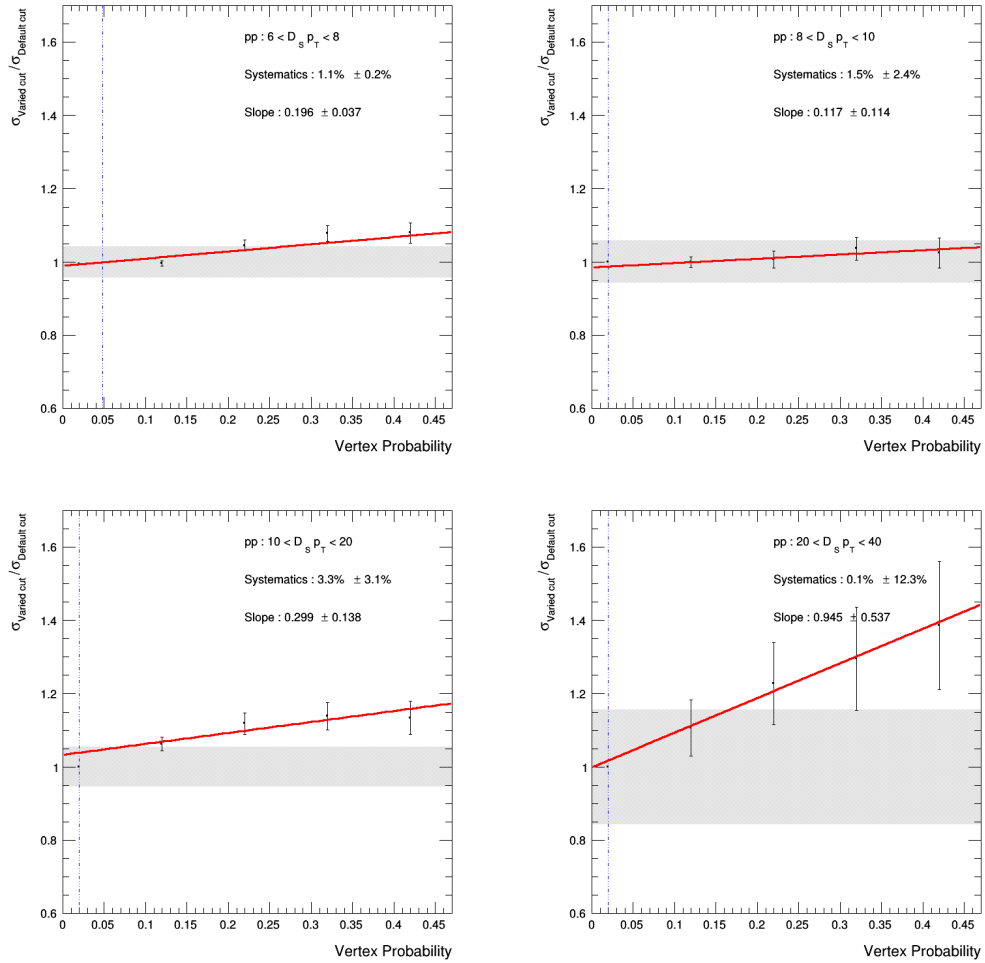


Figure 5.6. Vertex probability scan for D_s^+ with p_T range from 6 to 40 GeV/c in pp collisions, where the y-axis is the cross section ratio of varied cut to default cut. The blue dashed line indicate the default cut used in the analysis. The red dashed line is the linear fit of the data.

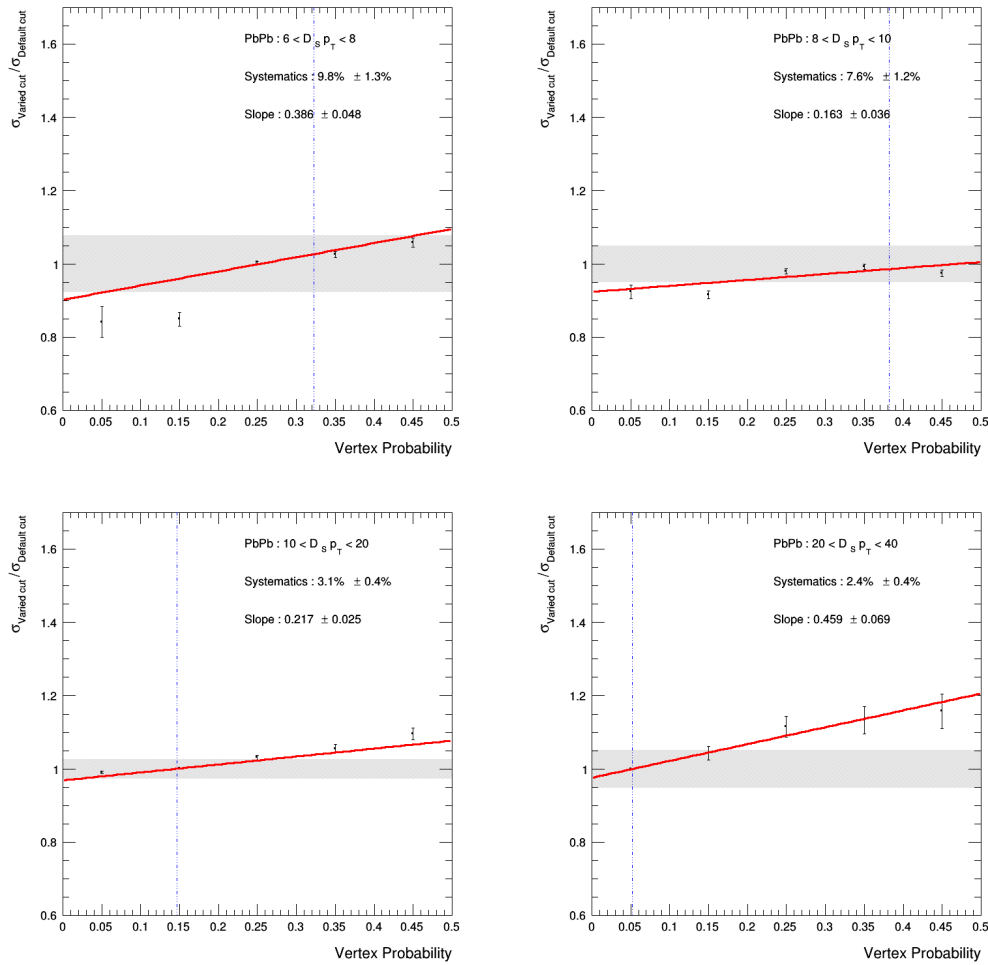


Figure 5.7. Vertex probability scan for D_s^+ with p_T range from 6 to 40 GeV/c in PbPb collisions, where the y-axis is the cross section ratio of varied cut to default cut. The blue dashed line indicate the default cut used in the analysis. The red dashed line is the linear fit of the data.

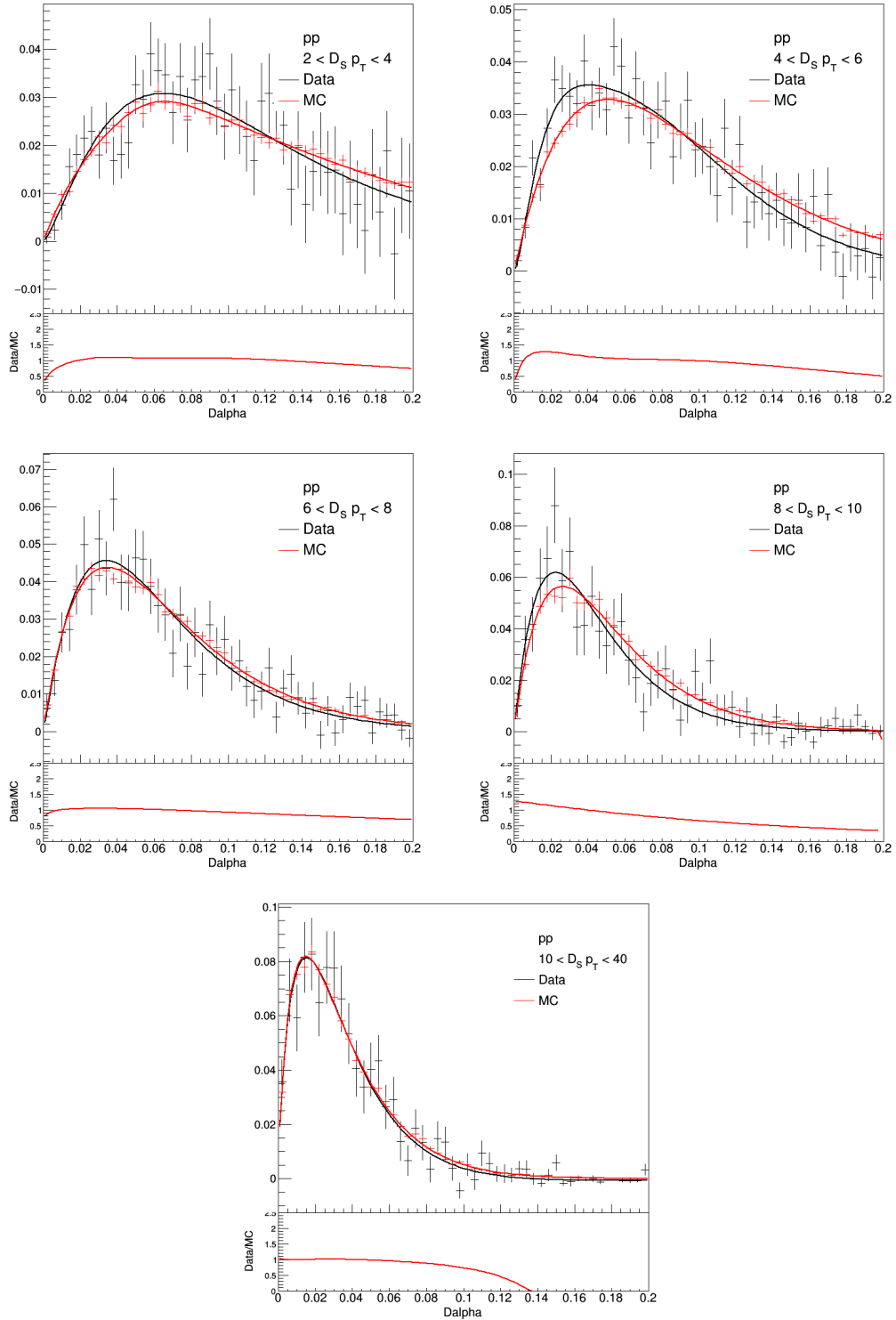


Figure 5.8. D_s^+ pointing angle distribution in data and MC (pp). Bottom panels: the ratio of data to MC.

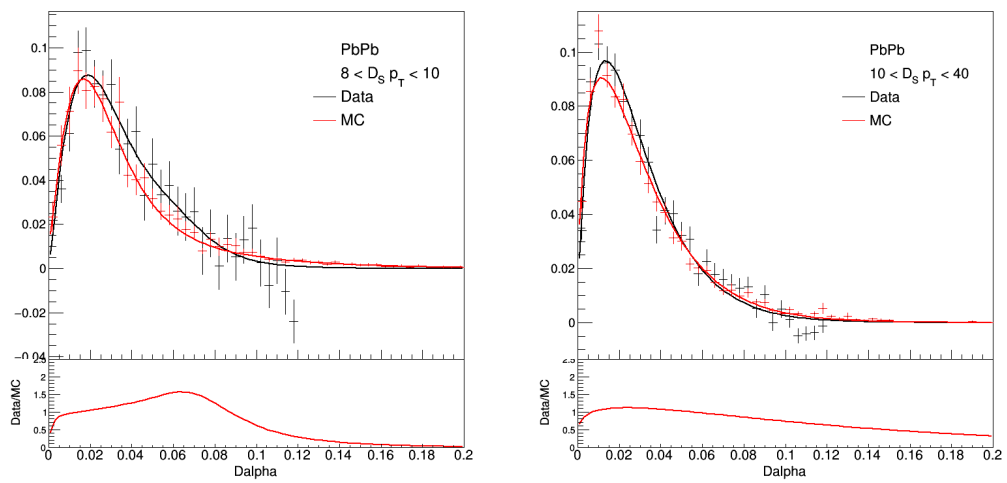


Figure 5.9. D_s^+ pointing angle distribution in data and MC (PbPb). Bottom panels: the ratio of data to MC.

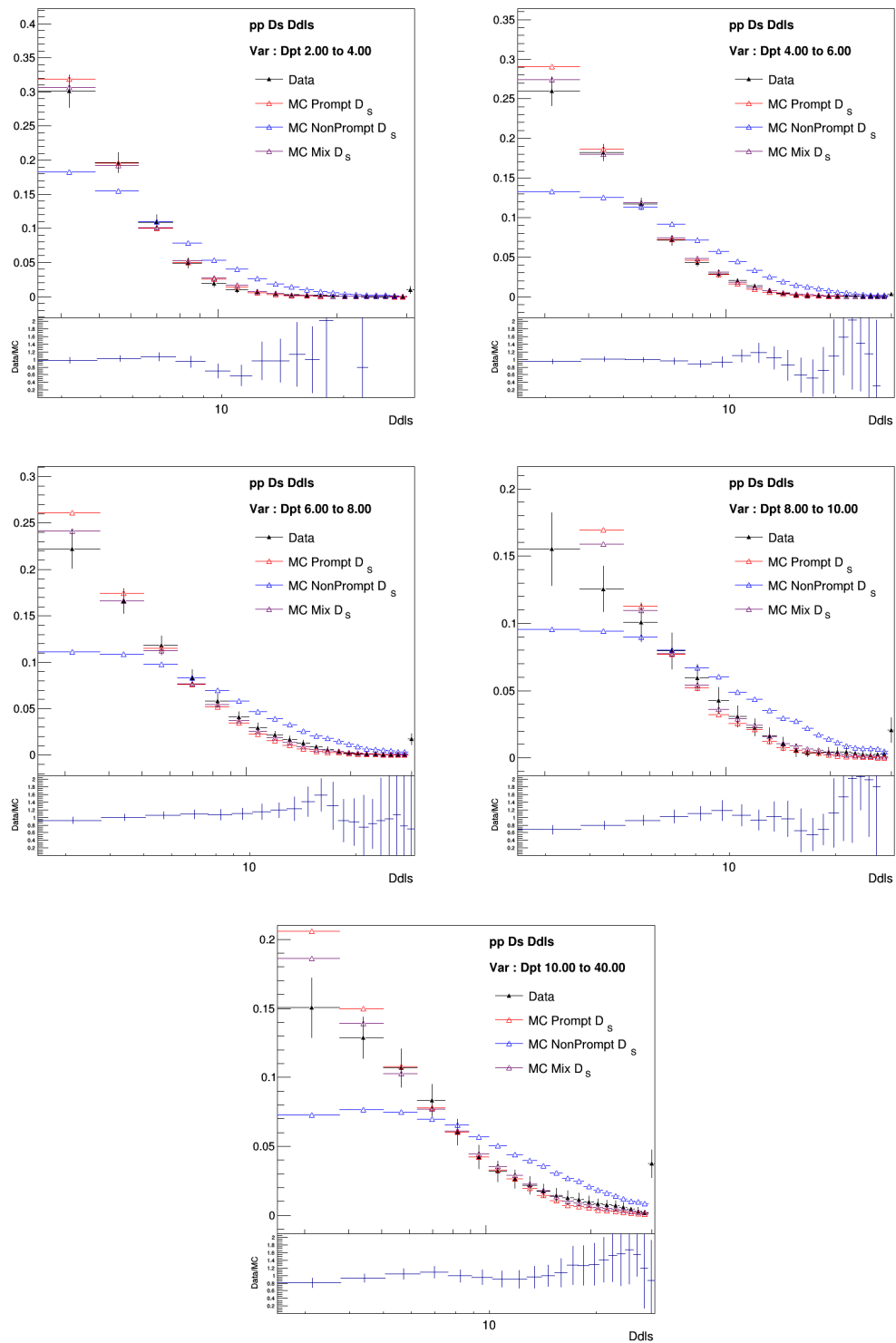


Figure 5.10. D_s^+ decay length significance in data and MC (pp). Bottom panels: the ratio of data to MC.

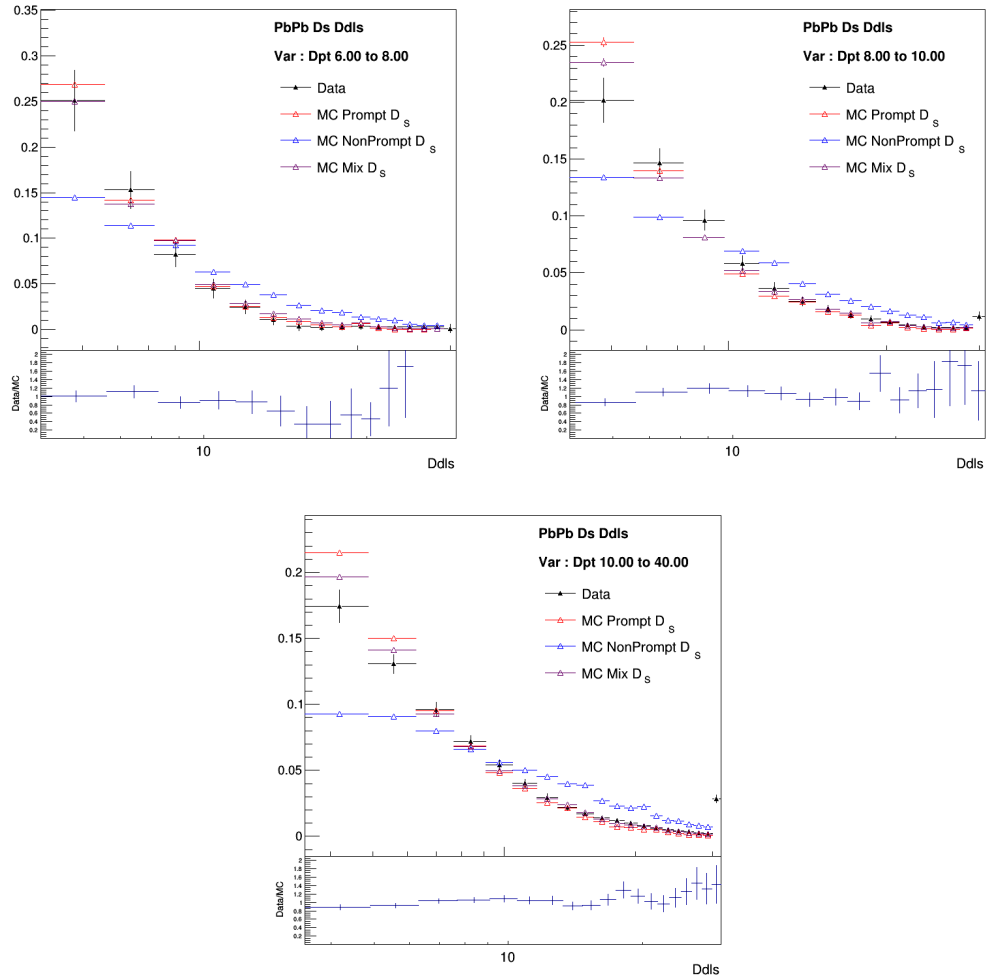


Figure 5.11. D_s^+ decay length significance in data and MC (PbPb). Bottom panels: the ratio of data to MC.

5.6 Systematics Associated with Signal Extraction

The systematic uncertainties associated with signal extraction are studied by changing the default fitting function to an alternative function. For background, the fitting function is changed to a second-order Chebyshev polynomial (and a third-order one for PbPb p_T 6-8 and 8-10 GeV/ c bins) shown in Figures 5.12 to 5.14. For signal, an alternative single-Gaussian function is used to compare with default double Gaussian fitting shown in Figures 5.15 to 5.17. The computed difference of fitted yield to the default value is taken as the systematics uncertainties. The total systematic for signal extraction is taking the quadrature sum of the signal function variation result and the background function variation result.

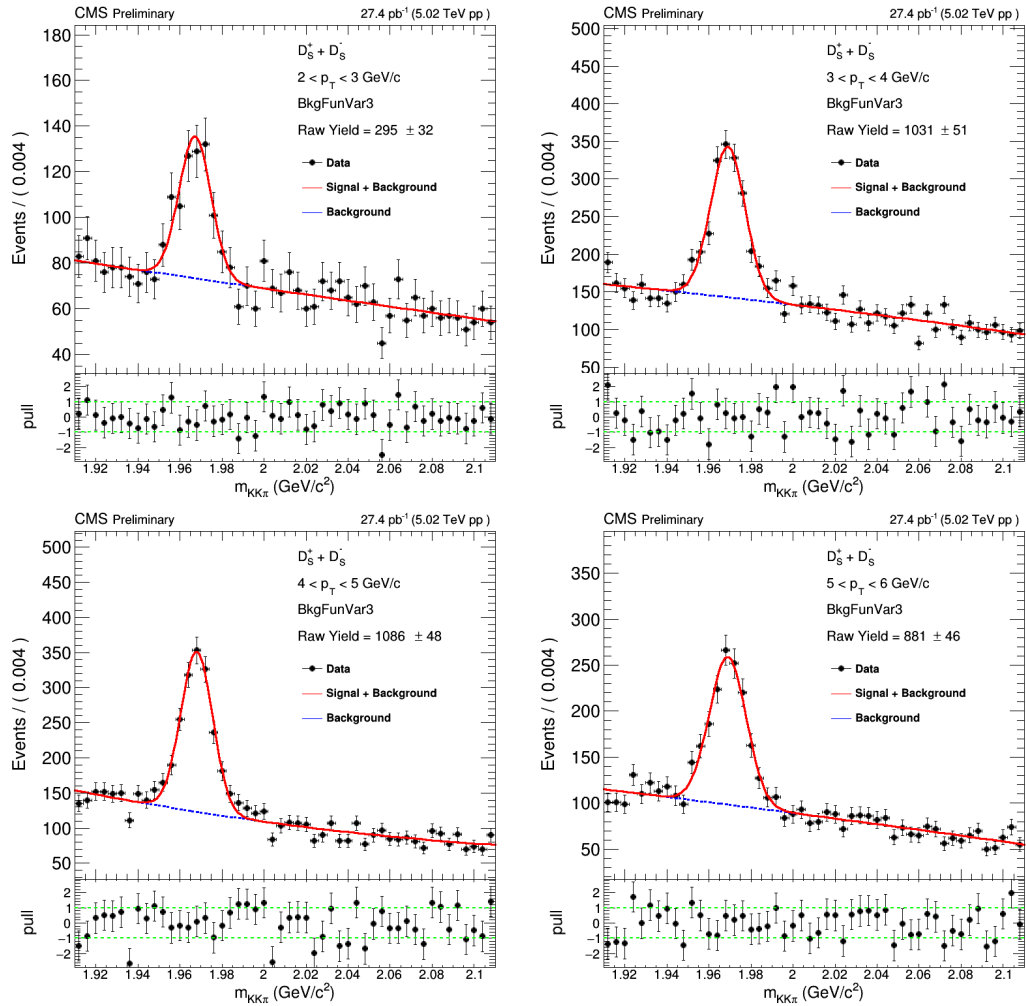


Figure 5.12. Signal extraction fit in pp collisions for $D_s^+ D_s^-$ p_T 2 to 6 GeV/c with second-order Chebyshev polynomial for background.

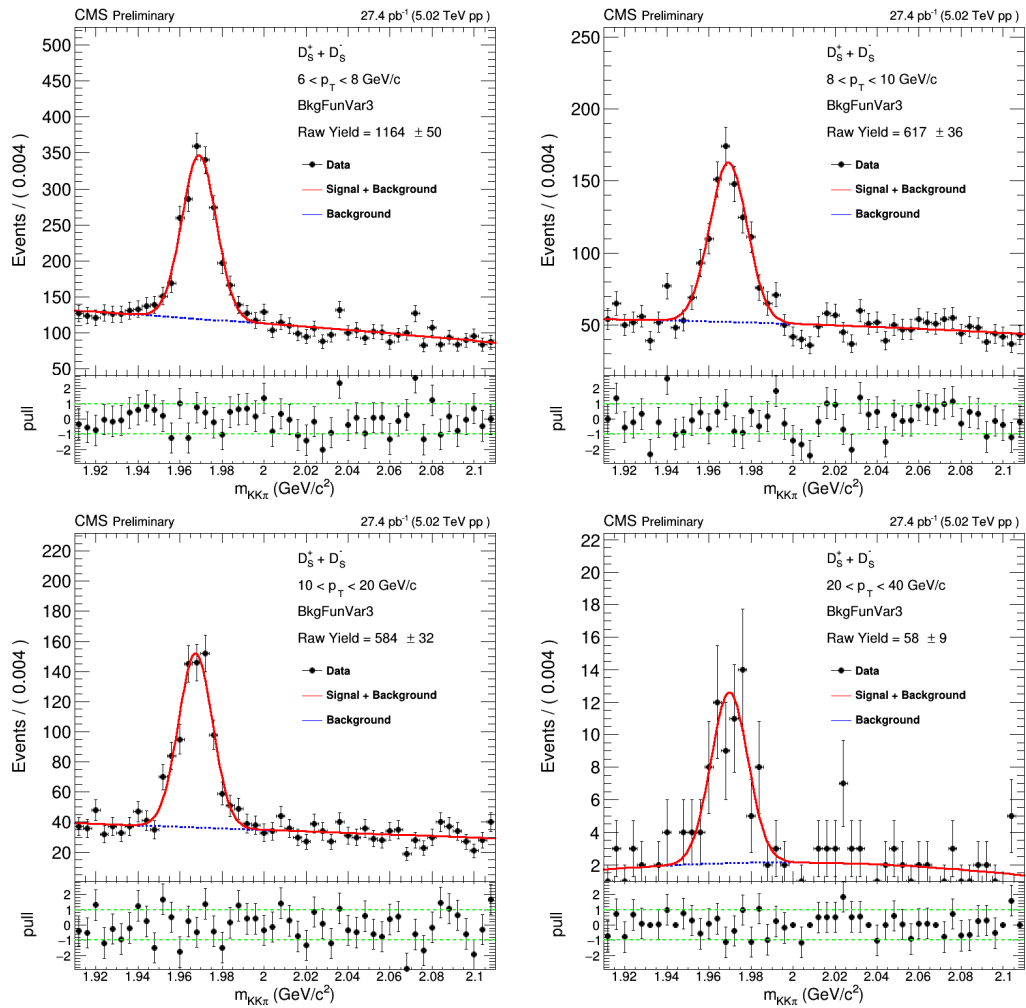


Figure 5.13. Signal extraction fit in pp collisions for $D_s^+ p_T$ 6 to 40 GeV/c with second-order Chebyshev polynomial for background.

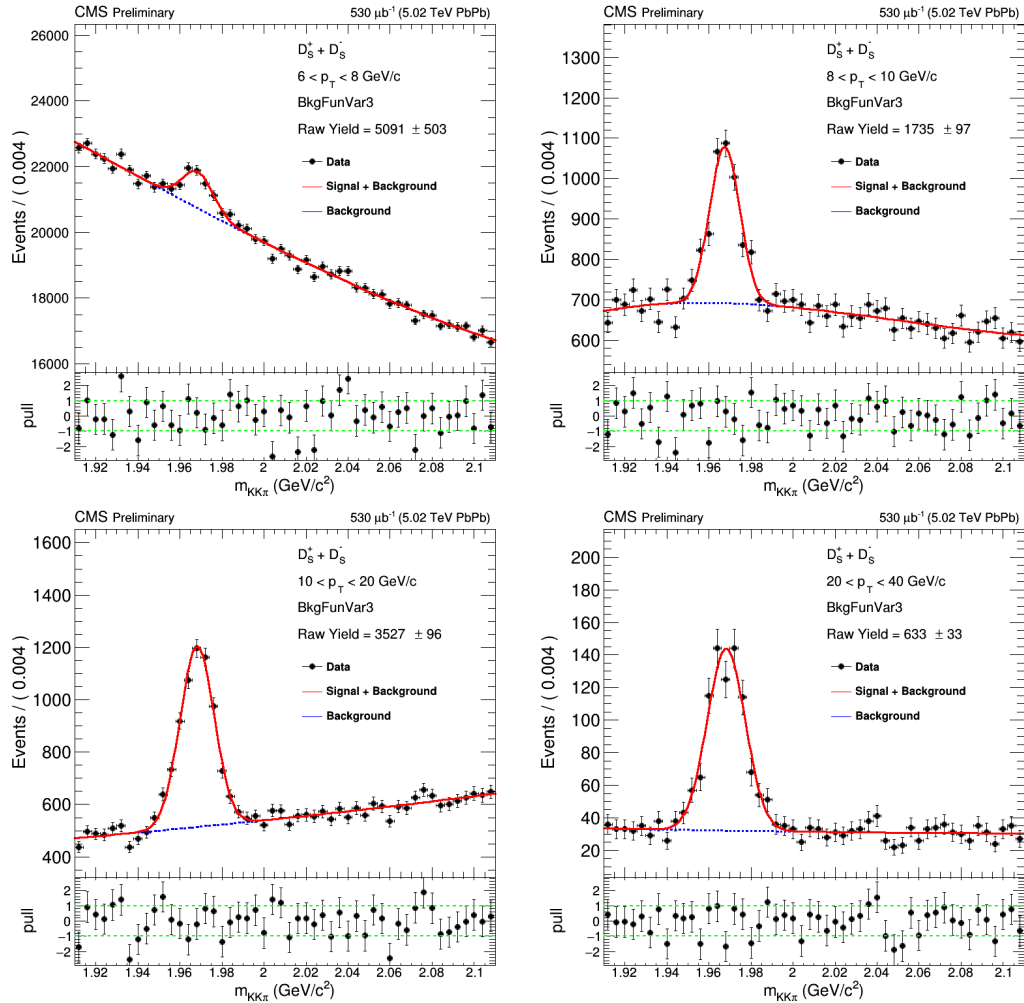


Figure 5.14. Signal extraction fit in PbPb collisions for D_s^+ p_T 6 to 40 GeV/c. Third-order Chebyshev polynomial for background in p_T : 6-8 and 8-10 GeV/c bins, and Second-order for background in p_T : 10-20 and 20-40 GeV/c bins .

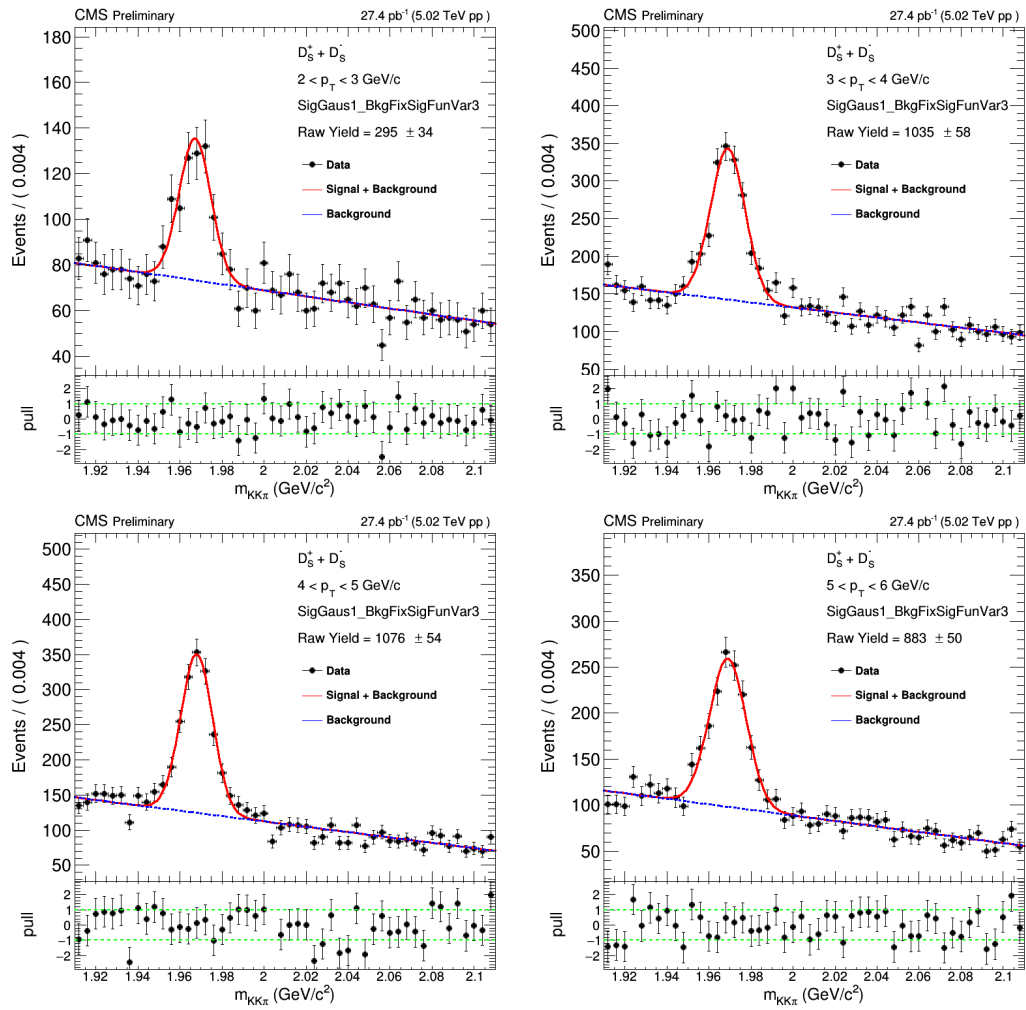


Figure 5.15. Signal extraction fit in pp collisions for $D_s^+ p_T$ 2 to 6 GeV/c with single-Gaussian fit for Signal.

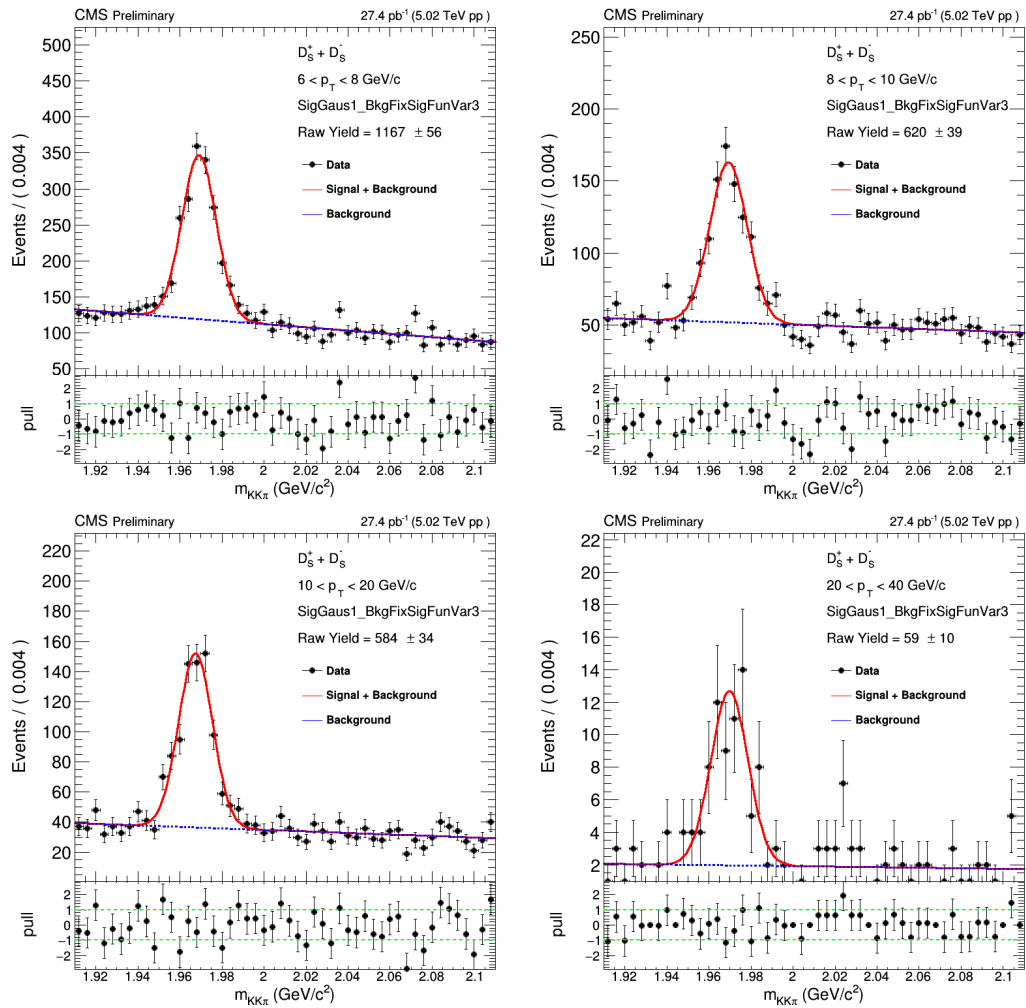


Figure 5.16. Signal extraction fit in pp collisions for $D_s^+ p_T$ 6 to 40 GeV/c with single-Gaussian fit for Signal.

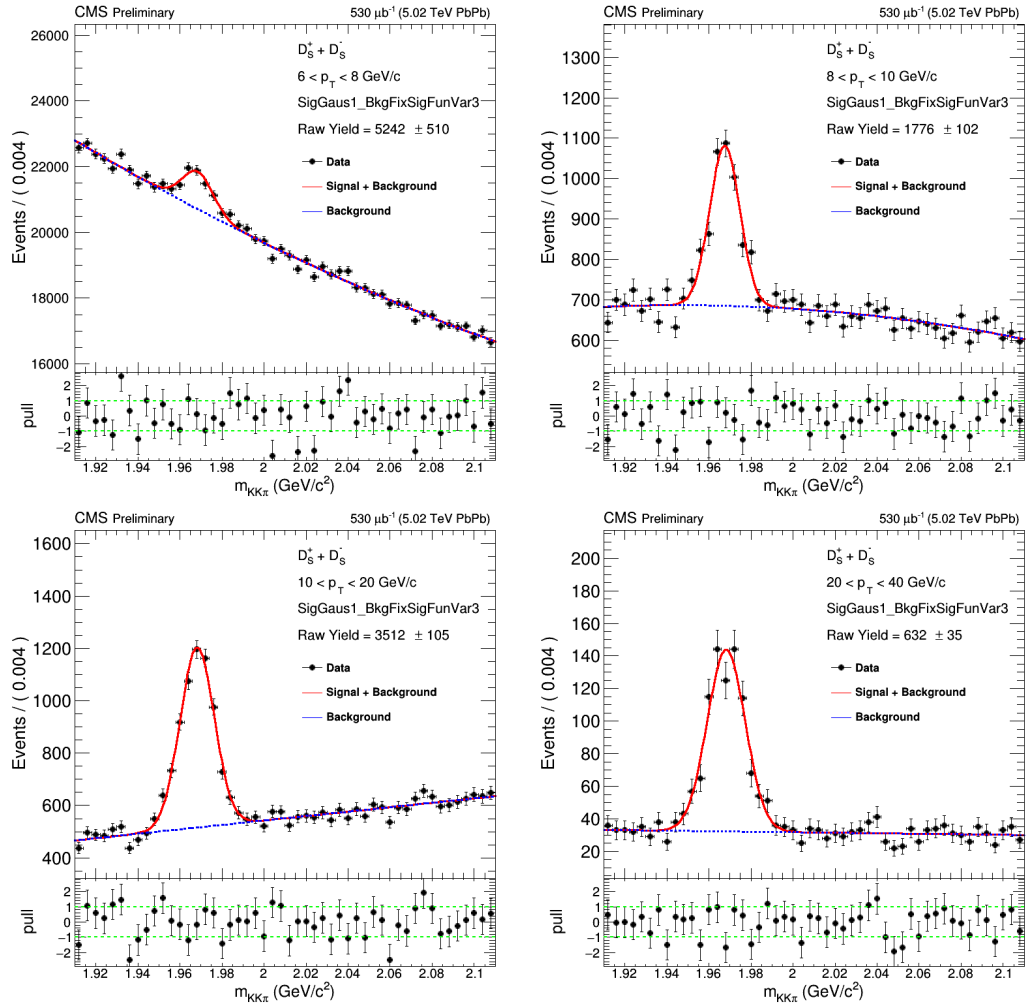


Figure 5.17. Signal extraction fit in PbPb collisions for D_s^+ p_T 6 to 40 GeV/c with single-Gaussian fit for Signal.

5.7 Systematic Associated with MC D_s^+ p_T Shape

The systematic uncertainty related to the MC p_T shape was evaluated by comparing the result from default weighted MC sample with FONLL based weighted MC sample. The details of MC weight is described in Section 3.3.1. Figure 5.18 shows the ratio of efficiency between alternative weight to default weight. The difference of differential cross section obtained by the alternative weight to the default is taken as the systematics.

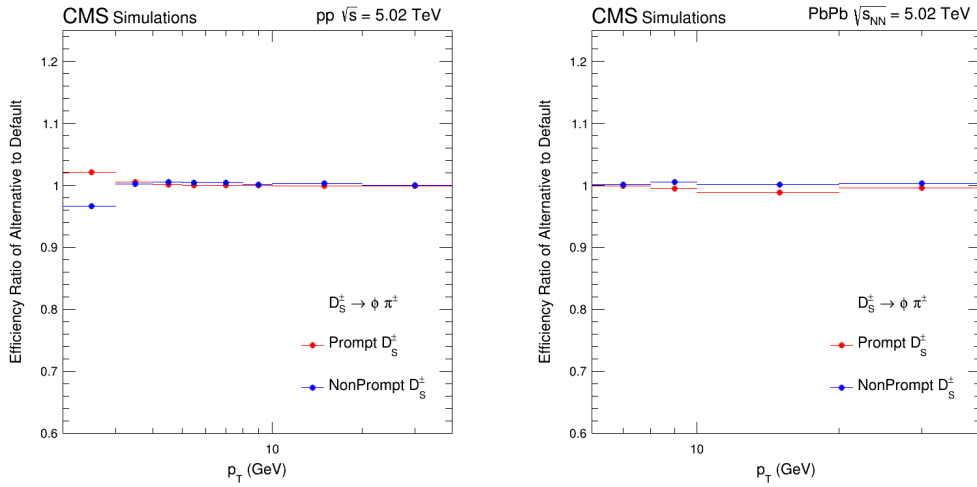


Figure 5.18. Ratio of efficiency for alternative weight to default weight for prompt D_s^+ (Red), non-prompt D_s^+ (blue) in pp(left) and PbPb(right) collisions.

5.8 Systematic Associated with Non-prompt Ds

Based on the method used to estimate the non-prompt D_s^+ , the systematics associated with it arose from the following sources : B fragmentation fraction, Branching fraction of B to D_s^+ and B to D^0 , the uncertainties in the Bto D^0 measurement, the D_s^+ p_T shape and the R_{AA} uncertainty for PbPb. The systematic of B fragmentation fraction is studied by using alternative fraction from CDF results(55) since it

is the result listed on PDG. The systematic of Branching fraction is estimated by adding or subtracting the one sigma of each terms separately , taking the larger one as systematics and sum over all terms in quadrature to be the total systematics. The default D_s^+ p_T shape is by applying the difference of D_s^+ and D^0 in MC simulation, the systematic is estimated by using the shape from FONLL Bpt distribution with the EVTGEN decay kinematics. The results are summarized in Table 5.8 and Table 5.9.

Table 5.8.
Relative systematics (%) for non-prompt D_s^+ in pp collisions.

Source	p_T interval (GeV)							
	2-3	3-4	4-5	5-6	6-8	8-10	10-20	20-40
B fraction	1.9	1.8	2.3	2.3	2.7	2.5	2.6	2.4
Branching Ratio	2.7	2.4	3.1	3.1	3.6	3.4	3.5	3.3
Bto D^0 uncertainty	3.9	2.8	3.1	3.3	2.6	3.6	3.7	2.7
D_s^+ p_T shape	0.5	1.6	3.7	1.5	2.3	0.6	3.2	1.5

Table 5.9.
Relative systematics (%) for non-prompt D_s^+ in PbPb collisions.

Source	p_T interval (GeV)			
	6-8	8-10	10-20	20-40
B fraction	4.3	5.6	5.5	3.3
Branching Ratio	5.9	7.6	7.5	4.5
Bto D^0 uncertainty	2.8	4.7	3.5	6.0
D_s^+ p_T shape	6.7	8.2	6.3	3.4

6. RESULTS AND SUMMARY

In this chapter, the measured results of p_T -differential cross section in pp and PbPb, nuclear modification factor, the production ratio of D_s^+ to D^0 are presented.

6.1 Results

The prompt D_s^+ p_T -differential cross section in each p_T interval in pp collisions ($d\sigma^{prompt D_s^+}/d_{p_T}$) can be computed using:

$$\frac{(N^{D_s^+ + D_s^-})|_{|y|<1} \cdot fr_\phi}{2 \cdot \mathcal{L} \cdot \Delta p_T} = \frac{d\sigma^{prompt D_s^+}}{dp_T} \Bigg|_{|y|<1} \cdot \mathcal{B}_\phi \cdot \epsilon_{prompt,\phi} + \frac{d\sigma^{nonprompt D_s^+}}{dp_T} \Bigg|_{|y|<1} \cdot \mathcal{B}_\phi \cdot \epsilon_{nonprompt,\phi}, \quad (6.1)$$

where the factor of 1/2 denotes the average of the measured particles and antiparticles, $N^{D_s^+ + D_s^-}$ is the extracted raw D_s^+ meson yield, fr_ϕ is the $D_s^+ \rightarrow \phi\pi^+ \rightarrow K^+K^-\pi^+$ channel ratio with respect to all sources, \mathcal{L} is the integrated luminosity, Δp_T is the width of the p_T interval, \mathcal{B}_ϕ is the branching fraction of the $D_s^+ \rightarrow \phi\pi^+ \rightarrow K^+K^-\pi^+$ decay chain, ϵ represents the acceptance and efficiency correction in each p_T interval, and $d\sigma^{nonprompt, D_s^+}/d_{p_T}$ is the p_T -differential cross section for nonprompt D_s^+ .

The prompt D_s^+ p_T -differential cross section in PbPb collisions ($1/T_{AA} \cdot dN^{prompt, D_s^+}/d_{p_T}$) can be computed using:

$$\frac{fr_\phi (N^{D_s^+ + D_s^-})|_{|y|<1}}{T_{AA} \cdot 2 \cdot N_{events} \cdot \Delta p_T} = \frac{1}{T_{AA}} \frac{d\sigma^{prompt D_s^+}}{dp_T} \Bigg|_{|y|<1} \cdot \mathcal{B}_\phi \cdot \epsilon_{prompt,\phi} + \frac{1}{T_{AA}} \frac{d\sigma^{nonprompt D_s^+}}{dp_T} \Bigg|_{|y|<1} \cdot \mathcal{B}_\phi \cdot \epsilon_{nonprompt,\phi}, \quad (6.2)$$

where the N_{events} is the number of minimum-bias events used in the analysis, T_{AA} is the nuclear overlap function equal to 5.61 mb^{-1} (56; 17), and $1/T_{AA} \cdot dN^{prompt, D_s^+}/dp_T$ is the p_T -differential cross section for nonprompt D_s^+ in PbPb collisions.

The prompt D_s^+ p_T -differential cross sections in the rapidity interval $|y| < 1$ in pp and PbPb collisions at $\sqrt{s_{NN}} = 5.02 \text{ TeV}$ are presented in Figure 6.1. The measured spectrum is for $2 < p_T < 40 \text{ GeV}/c$ for pp and $6 < p_T < 40 \text{ GeV}/c$ for PbPb. These results are compared with PYTHIA 8 with the data/PYTHIA ratio in the bottom panel. The measurement in pp shows a different p_T distribution than the PYTHIA prediction. At low p_T , the D_s^+ cross section is over-predicted by PYTHIA calculations, while at high p_T the PYTHIA calculations are smaller than the measured data.

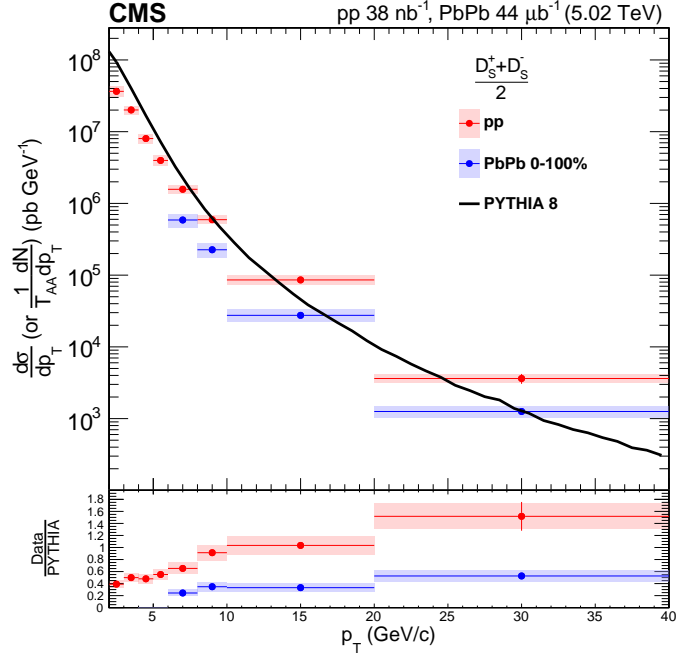


Figure 6.1. $\frac{d\sigma}{dp_T}$ in pp and $\frac{1}{T_{AA}} \frac{dN}{dp_T}$ in PbPb at $\sqrt{s_{NN}} = 5.02 \text{ TeV}$. The colored boxes represent the systematic uncertainty.

The D_s^+ nuclear modification factor (R_{AA}) is shown in Figure 6.2. The D_s^+ R_{AA} is between 0.35 to 0.40 in the p_T range from 6 GeV/c to 40 GeV/c , which indicates a

strong interaction between the charm quark and the QGP medium. Same observation has also been found in the D^0 measurement (12). The R_{AA} is compared with the PHSD calculation in the centrality range 0 – 80% (57; ?). PHSD is a microscopic off-shell transport model based on a Boltzmann approach that includes only collisional energy loss. The PHSD model is consistent with data within current measurement uncertainties.

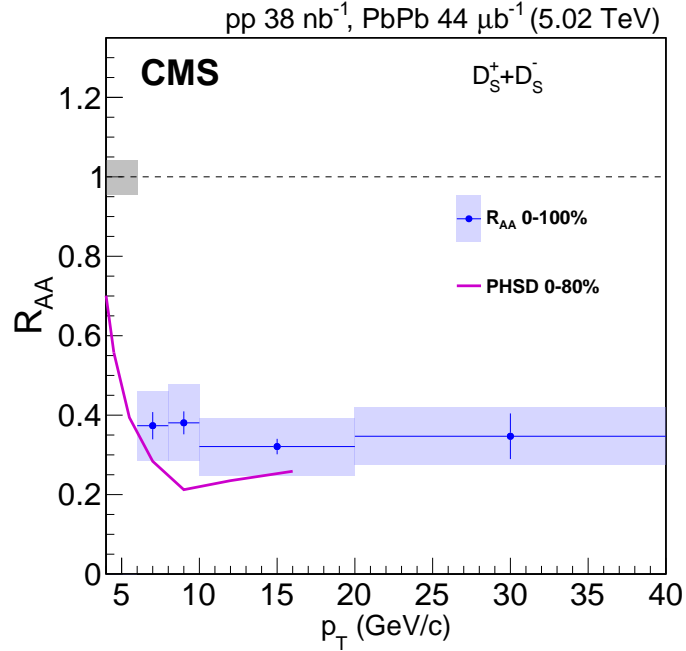


Figure 6.2. Nuclear modification factor (R_{AA}) of D_s^+ mesons in PbPb collisions at $\sqrt{s_{NN}} = 5.02$ TeV. The Magenta line represents the PHSD(43), the parton-hadron-string dynamics transport model including a contribution of hadronisation via quark recombination, prediction.

The ratios of prompt D_s^+/D^0 production in pp and PbPb are shown in Figure 6.2. The pp result shows a similar trend to the PYTHIA 8 prediction. However, the magnitude of the ratios is underpredicted by PYTHIA 8. While the PHSD pp prediction is similar to PYTHIA 8, the TAMU model (58), based on the statistical hadronization model with extra excited charm baryon states not listed in the current PDG,

demonstrates a larger D_s^+/D^0 ratio and a better match with data. The comparison of pp data with theory may suggest the need for including excited charm baryon states or may be an indication that coalescence plays an important role in pp collisions. The double ratios of D_s^+/D^0 in pp and PbPb are shown in the bottom panel of Figure 6.2 (right) and are consistent with unity. The PHSD model calculation, which includes the production through coalescence in PbPb collisions, reproduces the observed ratio.

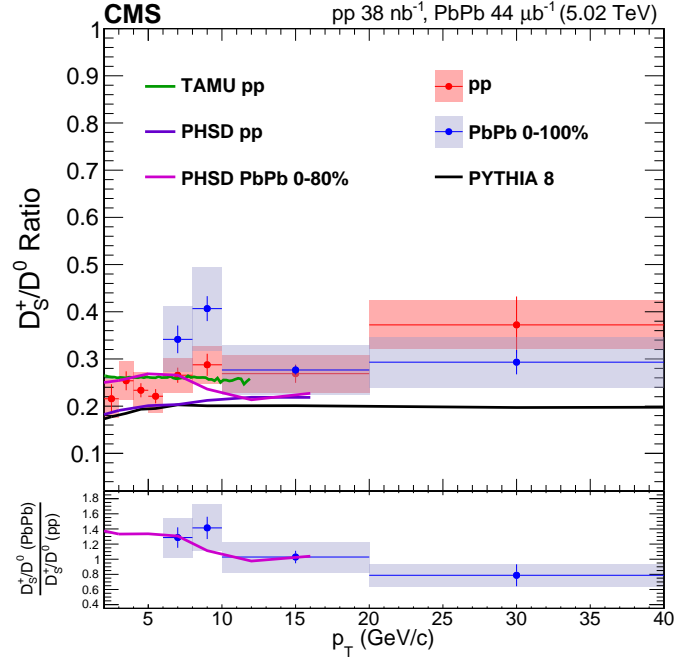


Figure 6.3. D_s^+/D^0 Ratio in pp and PbPb at $\sqrt{s_{NN}} = 5.02$ TeV. The lower panel shows the double ratio of D_s^+/D^0 in PbPb over in pp. The green line represents the TAMU(58), while the violet (magenta) line represents the PHSD pp (PbPb) prediction.

6.2 Summary

In this thesis, p_T -differential cross sections of prompt D_s^+ mesons and prompt D_s^+ nuclear modification factors in central rapidity ($|y| < 1$) in pp and PbPb collisions at

$\sqrt{s_{\text{NN}}} = 5.02$ TeV are presented. The prompt D_s^+ p_T -differential cross section in pp is found to be significantly lower than PYTHIA 8 calculations. The nuclear modification of prompt D_s^+ is below unity which indicates strong interaction between charm quarks and the QGP medium. The ratio of prompt D_s^+/D^0 in pp is consistent with PYTHIA 8 and model calculations. The double ratio of prompt D_s^+/D^0 in PbPb over pp is consistent with unity, which is in agreement with the PHSD calculation. The D_s^+ production in PbPb collisions do not show a significant enhancement relative to in pp collisions in the measured p_T range. Low p_T measurements with higher precision from the upcoming high-luminosity LHC heavy-ion runs could provide clearer information about charm quark hadronization from the QGP.

REFERENCES

REFERENCES

- David J. Gross and Frank Wilczek. Ultraviolet behavior of non-abelian gauge theories. *Phys. Rev. Lett.*, 30:1343–1346, Jun 1973.
- H. David Politzer. Reliable perturbative results for strong interactions? *Phys. Rev. Lett.*, 30:1346–1349, Jun 1973.
- Miklos Gyulassy and Larry McLerran. New forms of qcd matter discovered at rhic. *Nuclear Physics A*, 750(1):30 – 63, 2005. Quark-Gluon Plasma. New Discoveries at RHIC: Case for the Strongly Interacting Quark-Gluon Plasma. Contributions from the RBRC Workshop held May 14-15, 2004.
- Berndt Müller and James L. Nagle. Results from the relativistic heavy ion collider. *Annual Review of Nuclear and Particle Science*, 56(1):93–135, 2006.
- Observation of a centrality-dependent dijet asymmetry in lead-lead collisions at $\sqrt{s_{NN}} = 2.76$ TeV with the atlas detector at the lhc. *Phys. Rev. Lett.*, 105:252303, Dec 2010.
- Elliptic flow of charged particles in pb-pb collisions at $\sqrt{s_{NN}} = 2.76$ TeV. *Phys. Rev. Lett.*, 105:252302, Dec 2010.
- P. Bicudo, M. Cardoso, and N. Cardoso. Qcd confinement and chiral crossovers, two critical points, 2011.
- Szabolcs Borsányi, Zoltán Fodor, Christian Hoelbling, Sándor D. Katz, Stefan Krieg, Claudia Ratti, and Kálmán K. Szabó. Is there still any t c mystery in lattice qcd? results with physical masses in the continuum limit iii. *Journal of High Energy Physics*, 2010(9):73, 2010.
- Yuri L. Dokshitzer and D. E. Kharzeev. Heavy quark colorimetry of QCD matter. *Phys. Lett. B*, 519:199, 2001.
- Jaroslav Adam et al. Centrality dependence of high- p_T D meson suppression in Pb-Pb collisions at $\sqrt{s_{NN}} = 2.76$ TeV. *Journal of High Energy Physics*, 11:205, 2015.
- Jaroslav Adam et al. Transverse momentum dependence of D-meson production in Pb-Pb collisions at $\sqrt{s_{NN}} = 2.76$ TeV. *Journal of High Energy Physics*, 03:081, 2016.
- A.M. Sirunyan, A. Tumasyan, W. Adam, F. Ambroggi, and E. Asilar. Nuclear modification factor of D^0 mesons in PbPb collisions at $\sqrt{s_{NN}} = 5.02$ TeV. *Physics Letters B*, 782:474 – 496, 2018.

- L. Adamczyk, J. K. Adkins, G. Agakishiev, M. M. Aggarwal, Z. Ahammed, I. Alekseev, Y. Alford, Zoukarneeva, and M. Zyzak. Observation of D^0 Meson Nuclear Modifications in Au + Au Collisions at $\sqrt{s_{NN}} = 200$ GeV. *Phys. Rev. Lett.*, 113:142301, Sep 2014.
- A. M. Sirunyan, A. Tumasyan, W. Adam, F. Ambrogi, E. Asilar, T. Bergauer, J. Brandstetter, E. Brondolin, M. Dragicevic, J. Erö, M. N. Flechl, W. H. Smith, D. Taylor, and N. Woods. Measurement of Prompt D^0 Meson Azimuthal Anisotropy in Pb-Pb Collisions at $\sqrt{s_{NN}} = 5.02$ TeV. *Phys. Rev. Lett.*, 120:202301, May 2018.
- S. Acharya, D. Adamová, J. Adolfsson, M. M. Aggarwal, and Aglieri Rinella. D -Meson Azimuthal Anisotropy in Midcentral Pb-Pb Collisions at $\sqrt{s_{NN}} = 5.02$ TeV. *Phys. Rev. Lett.*, 120:102301, Mar 2018.
- L. Adamczyk, J. K. Adkins, G. Agakishiev, M. M. Aggarwal, Z. Ahammed, N. N. Ajitanand, I. Alekseev, D. M. Anderson, and Aoyama. Measurement of D^0 azimuthal anisotropy at midrapidity in Au + Au collisions at $\sqrt{s_{NN}} = 200$ GeV. *Phys. Rev. Lett.*, 118:212301, May 2017.
- Vardan Khachatryan et al. Charged-particle nuclear modification factors in PbPb and pPb collisions at $\sqrt{s_{NN}} = 5.02$ TeV. *JHEP*, 04:039, 2017.
- A. M. Sirunyan, A. Tumasyan, W. Adam, F. Ambrogi, E. Asilar, T. Bergauer, J. Brandstetter, and Dragicevic. Studies of Beauty Suppression via Nonprompt D^0 Mesons in Pb-Pb Collisions at $\sqrt{s_{NN}} = 5.02$ TeV. *Phys. Rev. Lett.*, 123:022001, Jul 2019.
- A. M. Sirunyan, A. Tumasyan, W. Adam, E. Asilar, T. Bergauer, and Brandstetter. Measurement of the B^\pm Meson Nuclear Modification Factor in Pb-Pb Collisions at $\sqrt{s_{NN}} = 5.02$ TeV. *Phys. Rev. Lett.*, 119:152301, Oct 2017.
- Johann Rafelski and Berndt Muller. Strangeness Production in the Quark - Gluon Plasma. *Phys. Rev. Lett.*, 48:1066, 1982. [Erratum: *Phys. Rev. Lett.*56,2334(1986)].
- G. Agakishiev, M. M. Aggarwal, Z. Ahammed, A. V. Alakhverdyants, I. Alekseev, J. Alford, B. D. Anderson, C. D. Anson, D. Arkhipkin, and G. S. Averichev. Strangeness Enhancement in Cu-Cu and Au-Au Collisions at $\sqrt{s_{NN}} = 200$ GeV. *Phys. Rev. Lett.*, 108:072301, Feb 2012.
- B. I. Abelev, M. M. Aggarwal, Z. Ahammed, B. D. Anderson, D. Arkhipkin, G. S. Averichev, Y. Bai, J. Balewski, O. Barannikova, L. S. Barnby, J. Baudot, S. Baumgart, D. R. Beavis, R. Bellwied, and F. Benedosso. Enhanced strange baryon production in Au+Au collisions compared to $p + p$ at $\sqrt{s_{NN}} = 200$ GeV. *Phys. Rev. C*, 77:044908, Apr 2008.
- B. Abelev, J. Adam, D. Adamová, A.M. Adare, M.M. Aggarwal, G. Aglieri Rinella, M. Agnello, and A.G. Agocs. Multi-strange baryon production at mid-rapidity in Pb-Pb collisions at $\sqrt{s_{NN}} = 2.76$ TeV. *Physics Letters B*, 728:216 – 227, 2014.
- V. Greco, C. M. Ko, and P. Lévai. Partonic coalescence in relativistic heavy ion collisions. *Phys. Rev. C*, 68:034904, Sep 2003.

V. Greco, C.M. Ko, and R. Rapp. Quark coalescence for charmed mesons in ultra-relativistic heavy-ion collisions. *Physics Letters B*, 595(1):202 – 208, 2004.

Inga Kuznetsova and Johann Rafelski. Charmed hadrons from strangeness-rich QGP. *Journal of Physics G: Nuclear and Particle Physics*, 32(12):S499–S504, nov 2006.

A.M. Sirunyan, A. Tumasyan, W. Adam, F. Ambrogio, E. Asilar, and T. Bergauer and N. Woods. Measurement of B_s^0 meson production in pp and PbPb collisions at $\sqrt{s_{NN}} = 5.02$ TeV. *Physics Letters B*, 796:168 – 190, 2019.

S. Acharya, F.T. Acosta, D. Adamová, S.P. Adhya, A. Adler, J. Adolfsson, M.M. Aggarwal, G. Aglieri Rinella, M. Agnello, N. Agrawal, Z. Ahammed, S. Ahmad, S.U. Ahn, S. Aiola, A. Akindinov, M. Al-Turany, S.N. Alam, D.S.D. Albuquerque, D. Aleksandrov, B. Alessandro, H.M. Alfanda, R. Alfaro Molina, Y. Ali, A. Alici, A. Alkin, J. Alme, T. Alt, and L. Altenkamper. Λ_c^+ production in Pb-Pb collisions at $\sqrt{s_{NN}} = 5.02$ TeV. *Physics Letters B*, 793:212 – 223, 2019.

Lyndon Evans and Philip Bryant. Lhc machine. *Journal of Instrumentation*, 3(08):S08001, 2008.

The ATLAS Collaboration, G Aad, E Abat, J Abdallah, A A Abdelalim, A Abdeslam Perus, V D Peshekhonov, E Petereit, J Petersen, T C Petersen, P J F Petit, C Petridou, E Petrolo, F Petrucci, R Petti, M Pezzetti, B Pfeifer, A Phan, A W Phillips, and P W Phillips. The ATLAS experiment at the CERN large hadron collider. *Journal of Instrumentation*, 3(08):S08003–S08003, aug 2008.

S Chatrchyan et al. The cms experiment at the cern lhc. *Journal of Instrumentation*, 3(08):S08004, 2008.

The ALICE Collaboration, K Aamodt, A Abrahantes Quintana, R Achenbach, S Acounis, D Adamová, C Adler, M Aggarwal, F Agnese, G Aglieri Rinella, Z Ahammed, A Zhalov, D Zhou, S Zhou, G Zhu, A Zichichi, A Zinchenko, G Zinoviev, Y Zoccarato, A Zubarev, A Zucchini, and M Zuffa. The ALICE experiment at the CERN LHC. *Journal of Instrumentation*, 3(08):S08002–S08002, aug 2008.

Pierre Billoir. Progressive track recognition with a kalman-like fitting procedure. *Computer Physics Communications*, 57(1):390 – 394, 1989.

Serguei Chatrchyan et al. Description and performance of track and primary-vertex reconstruction with the CMS tracker. *JINST*, 9:P10009, 2014.

CMS Heavy Ion. Centrality and event plane reconstruction for pbb collisions at 5 tev in 2015. CMS Analysis Note AN-15-080, CMS, 2015.

Vardan Khachatryan et al. Transverse momentum and pseudorapidity distributions of charged hadrons in pp collisions at $\sqrt{s} = 0.9$ and 2.36 TeV. *JHEP*, 02:041, 2010.

Torbjörn Sjöstrand, Stefan Ask, Jesper R. Christiansen, Richard Corke, Nishita Desai, Philip Ilten, Stephen Mrenna, Stefan Prestel, Christine O. Rasmussen, and Peter Z. Skands. An Introduction to PYTHIA 8.2. *Comput. Phys. Commun.*, 191:159, 2015.

D.J. Lange. The EvtGen particle decay simulation package. *Nucl.Instrum.Meth.*, A462:152–155, 2001.

E. Barberio, B. van Eijk, and Z. Was. Photos – a universal Monte Carlo for QED radiative corrections in decays. *Comput. Phys. Commun.*, 66:115, 1991.

I. P. Lokhtin and A. M. Snigirev. A model of jet quenching in ultrarelativistic heavy ion collisions and high- p_T hadron spectra at RHIC. *Eur. Phys. J. C*, 45:211, 2006.

Studies of beauty suppression via measurements of nonprompt D^0 mesons in PbPb collisions at $\sqrt{s_{NN}} = 5.02\text{TeV}$. Technical Report CMS-PAS-HIN-16-016, CERN, Geneva, 2018.

Matteo Cacciari, Mario Greco, and Paolo Nason. The P(T) spectrum in heavy flavor hadroproduction. *JHEP*, 05:007, 1998.

Taeso Song, Hamza Berrehrah, Daniel Cabrera, Wolfgang Cassing, and Elena Bratkovskaya. Charm production in Pb + Pb collisions at energies available at the CERN Large Hadron Collider. *Phys. Rev. C*, 93:034906, Mar 2016.

Min He, Rainer J. Fries, and Ralf Rapp. Heavy-quark diffusion and hadronization in quark-gluon plasma. *Phys. Rev. C*, 86:014903, Jul 2012.

Min He, Rainer J. Fries, and Ralf Rapp. Heavy flavor at the large hadron collider in a strong coupling approach. *Physics Letters B*, 735:445 – 450, 2014.

M. Tanabashi and K. et.al Hagiwara. Review of particle physics. *Phys. Rev. D*, 98:030001, Aug 2018.

Kirill Prokofiev and T. Speer. A kinematic and a decay chain reconstruction library. In *Computing in high energy physics and nuclear physics. Proceedings, Conference, CHEP'04, Interlaken, Switzerland, September 27-October 1, 2004*, pages 411–414, 2005.

K. Prokofiev, Th. Speer. A kinematic fit and a decay chain reconstruction library. CMS Internal Note IN-2004-020, CMS, 2004.

Helge Voss, Andreas Höcker, Jörg Stelzer, and Frerik Tegenfeldt. TMVA, the toolkit for multivariate data analysis with ROOT. In *XIth International Workshop on Advanced Computing and Analysis Techniques in Physics Research (ACAT)*, page 40, 2007.

Wouter Verkerke and David P. Kirkby. The RooFit toolkit for data modeling. *eConf*, C0303241:MOLT007, 2003. [,186(2003)].

R Aaij et al. Measurement of B meson production cross-sections in proton-proton collisions at $\sqrt{s} = 7\text{ TeV}$. *JHEP*, 08:117, 2013.

CMS Collaboration. D^0 meson nuclear modification factor in PbPb collisions at $\sqrt{s_{NN}} = 5.02\text{ TeV}$. 2016.

CMS Luminosity Calibration for the pp Reference Run at $\sqrt{s} = 5.02\text{ TeV}$. Technical Report CMS-PAS-LUM-16-001, CERN, Geneva, 2016.

M. Pivk and F.R. Le Diberder. Plots: A statistical tool to unfold data distributions. *Nuclear Instruments and Methods in Physics Research Section A: Accelerators, Spectrometers, Detectors and Associated Equipment*, 555(1):356 – 369, 2005.

Y. Amhis and Sw et.al Banerjee. Averages of b-hadron, c-hadron, and tau-lepton properties as of summer 2016. *The European Physical Journal C*, 77(12):895, Dec 2017.

Michael L. Miller, Klaus Reygers, Stephen J. Sanders, and Peter Steinberg. Glauber modeling in high energy nuclear collisions. *Ann. Rev. Nucl. Part. Sci.*, 57:205, 2007.

Taesoo Song, Hamza Berrehrah, Daniel Cabrera, Juan M. Torres-Rincon, Laura Tolos, Wolfgang Cassing, and Elena Bratkovskaya. Tomography of the quark-gluon plasma by charm quarks. *Phys. Rev. C*, 92:014910, Jul 2015.

Min He and Ralf Rapp. Charm-baryon production in proton-proton collisions. *Physics Letters B*, 795:117 – 121, 2019.